Scientific Research Publishing

Open Journal of Air Pollution, 2026, 15(1), 1-31
https://www.scirp.org/journal/ojap
ISSN Online: 2169-2661
ISSN Print: 2169-2653

Three-Dimensional Analytical Modeling of Carbon Monoxide Dispersion over the Gulf of Guinea with 4D-Var Data Assimilation

Vincent Nounassou Hounkpe[1*], Kossi François Guedje[1,2], Joseph A. Adéchinan[3], Arnaud V. Houeto[2], Thomas D'Aquin Allagbe[1,2]

[1]International Chair in Mathematical Physics and Applications (ICMPA), University of Abomey-Calavi, Abomey-Calavi, Benin
[2]Laboratory of Materials Science and Modelling, Faculty of Science and Technology (FAST), University of Abomey-Calavi, Abomey-Calavi, Benin
[3]National School of Mathematical Engineering and Modelling (ENSGMM), National University of Science, Technology, Engineering and Mathematics, Abomey, Benin
Email: *hounkpevincent@gmail.com

How to cite this paper: Hounkpe, V.N., Guédjé, K.F., Adéchinan, J.A., Houeto, A.V. and Allagbe, T.D. (2026) Three-Dimensional Analytical Modeling of Carbon Monoxide Dispersion over the Gulf of Guinea with 4D-Var Data Assimilation. *Open Journal of Air Pollution*, **15**, 1-31.
https://doi.org/10.4236/ojap.2026.151001

Received: January 30, 2026
Accepted: March 27, 2026
Published: March 30, 2026

Abstract

Atmospheric dispersion modelling in West Africa is crucial to understand, predict, and mitigate the impacts of air pollution on public health, ecosystems, and regional climate in a context of rapid urbanization and industrialization. This study develops a three-dimensional analytical model for carbon monoxide (CO) dispersion, governed by the turbulent scalar flux transport equation within a second-order Eulerian framework. A theoretical analysis of the model establishes the existence and uniqueness of the solution, and derives the associated optimality system using control theory and monotone operator techniques. From this formulation, an analytical solution is obtained that explicitly incorporates diffusion coefficients, turbulence intensities dependent on atmospheric stability (cloud cover and radiation), and three-dimensional wind components (u, v, w) derived from ERA5 reanalysis. The analytical model is then calibrated through four-dimensional variational data assimilation (4D-Var) using satellite-based CO observations from the Copernicus EAC4 reanalysis, to produce fields consistent with observations. An application over the Gulf of Guinea during the dry season demonstrates that the coupled Model-4D-Var system generates CO dispersion maps with finer spatial resolution ($0.25^\circ \times 0.25^\circ$) than the input satellite products ($0.75^\circ \times 0.75^\circ$), while maintaining good agreement with observations, as indicated by low RMSE, small negative fractional bias, and FAC2 values between 0.5 and 2 at most pressure levels. These high-resolution maps enable the quantification, identification, and tracking of CO plumes in space and time, including persistent plumes over southern and northern Nigeria, Ghana, and the Central African Republic,

linked to gas flaring, biomass burning, and urban/industrial emissions. The results highlight the potential of combining an analytical dispersion model with 4D-Var to improve CO monitoring in data-sparse regions, such as the Gulf of Guinea.

Keywords

Carbon Monoxide, 4D-Var Data Assimilation, ERA5, EAC4, Gulf of Guinea

1. Introduction

Air pollution is a leading cause of morbidity and premature mortality worldwide and represents a major environmental and public health challenge at the global scale [1]. Numerous anthropogenic and natural sources contribute to atmospheric pollution, including fossil fuel combustion, biomass burning, gas flaring, forest fires, road traffic, residential heating, and industrial activities [1]-[4]. Emissions from biomass burning, in particular, contain large amounts of gaseous compounds and particles that significantly affect local, regional and even global air quality [5]. Among the emitted species, carbon monoxide (CO) plays a key role in controlling the oxidative capacity of the troposphere through its reaction with the hydroxyl radical (OH), and thereby influences ozone formation and loss depending on nitrogen oxide (NO_x) levels [6]. Typical CO lifetimes of several weeks allow long-range transport and regional accumulation, especially in the tropics [7].

In West Africa, and more specifically over the Gulf of Guinea, CO originates from both natural and anthropogenic sources, including agricultural fires, savanna and forest fires, domestic combustion, and gas flaring associated with oil and gas production [4] [8]-[10]. Nigeria is among the most affected countries due to intensive flaring and rapid urbanization, with cities such as Onitsha and Kaduna reported among the most polluted worldwide in terms of particulate matter [1] [11] [12]. Other coastal and inland countries (Ghana, Côte d'Ivoire, Burkina Faso, Niger, Togo, Benin) also contribute through industrial emissions, road transport, domestic fires and biomass burning [10] [13]. In addition, long-range transport of dust from the Sahara-Sahel region and biomass-burning plumes from Central Africa further enhances pollution levels over the Gulf of Guinea, particularly during the dry season (December-February) [8] [13] [14].

Despite this strong pollution burden, air quality modeling over West Africa remains among the least developed in the world, owing to limited observational networks, scarce emission inventories, and reduced computational and financial resources [12] [13]. Atmospheric dispersion modeling is inherently complex, as it requires accounting for a wide range of physical and chemical processes, including advection, turbulent diffusion, boundary-layer dynamics, and, where relevant, chemical transformation [15]. While several observation networks and campaigns (e.g. AERONET, AMMA, DACCIWA) have improved our understanding of aer-

osols and trace gases in the region [8] [13], few studies have addressed the explicit modeling of CO dispersion at regional scale over the Gulf of Guinea [4] [16]. Understanding the spatio-temporal dynamics of CO plumes in this region, therefore remains a challenging and partly open problem.

In this study, we focus on quantifying and characterizing CO dispersion over the Gulf of Guinea using a physically-based yet computationally efficient modeling framework. We develop a three-dimensional analytical dispersion model derived from the complete turbulent scalar flux transport equation (Differential Flux Model, DFM) [17], which accounts for horizontal and vertical diffusion under stability-dependent turbulence parameterizations. The model is driven by ERA5 reanalysis meteorological fields [18] and is coupled with a four-dimensional variational (4D-Var) data assimilation scheme used to adjust the initial CO concentration based on satellite-derived CO data from the ECMWF Atmospheric Composition Reanalysis 4 (EAC4) [19].

The main contributions of this work are threefold. First, we derive and analyze a 3D analytical solution for CO concentration, including a theoretical study of existence, uniqueness and optimality using monotone operator theory and optimal control [20]-[22]. Second, we implement a 4D-Var assimilation framework that constrains the analytical model with ERA5 meteorology and EAC4 CO, and we evaluate its performance using standard statistical metrics (RMSE, fractional bias, FAC2) [23] [24]. Third, we apply the coupled system over the Gulf of Guinea to identify and track major CO plumes associated with gas flaring, urban emissions, and biomass burning, and we discuss the role of regional wind regimes and atmospheric stability in shaping their dispersion [2] [4] [8].

The paper is organized as follows. Section 2 describes the study area, data and methods, including the analytical formulation and the 4D-Var setup. Section 3 presents the numerical experiments, validation results, and analysis of CO plumes. Section 4 summarizes the main findings and outlines perspectives for future improvements and applications.

2. Study Area, Data and Methods

2.1. Study Area

The study focuses on coastal areas, specifically in the Gulf of Guinea (**Figure 1**), which extends from 4˚S to 18˚N and from −10˚W to 20˚E. It represents 50% of the continent's pollution and 10% globally [11]. The study area is characterized by two seasons: the rainy season and the dry season. The long dry season extends from December to February; the short dry season, from July to September. As for the rainy season, the long rainy season occurs from May to June and begins in March-April; the short rainy season, from October to November [25]. The West African region is characterized by four types of wind regimes: *the monsoon and Harmattan winds*, *the nocturnal low-level jet* (*NLLJ*) *and the land-sea breeze* (*LSB*) *system* [25]. These different wind regimes play a crucial role in the redistribution of pollutants emitted by coastal area cities [25].

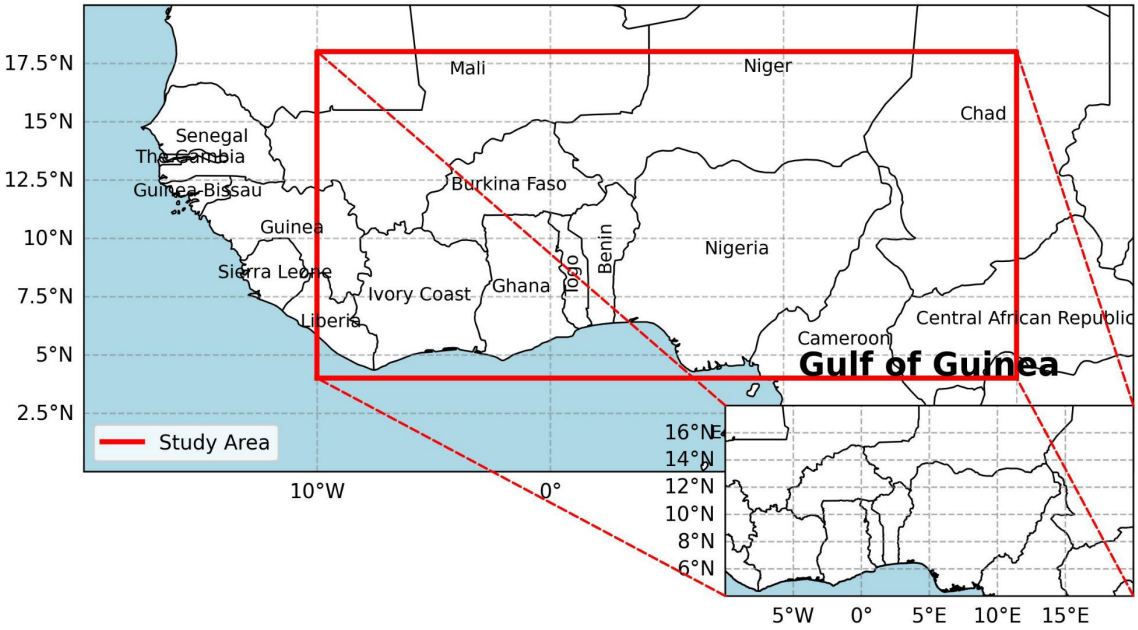

Figure 1. The image shown here delimits the study area by highlighting coastal countries with a black line.

However, we denote $\mathcal{Q}$ the study area with a spatial resolution of 0.25˚ × 0.25˚ (approximately 28 km × 28 km) and a temporal resolution of three hours. It is distributed according to latitude, longitude, and pressure level (altitude). Each point on the grid, according to the pressure level, has an area of 28 km × 28 km.

2.2. Data

In this study, we used meteorological data from the *ERA*5 reanalysis developed by the *European Centre for Medium-Range Weather Forecasts* (*ECMWF*) [18]. This data is accessible via the following link: https://cds.climate.copernicus.eu/. It is characterized by a spatial resolution of 0.25˚ × 0.25˚ and three-hourly temporal resolution. These meteorological data are presented in Table 1. TOA incident radiation, fraction of cloud cover and friction velocity are defined without pressure levels.

Table 1. Meteorological variables (*ERA*5).

Name	Variables	Vertical levels (hPa)
Zonal wind velocity	U (m·s^{-1})	1000, 950, 900, 850, 800
Meridional wind velocity	V (m·s^{-1})	1000, 950, 900, 850, 800
Vertical wind velocity	W (m·s^{-1})	1000, 950, 900, 850, 800
Temperature	T (K)	1000, 950, 900, 850, 800
Friction velocity	*zust* (m·s^{-1})	Independent of pressure levels
Fraction of cloud cover	*cc*	1000, 950, 900, 850, 800
TOA incident radiation	*tisr* (J·m^{-2})	Independent of pressure levels
Convective available potential energy	*cape* (J·kg^{-1})	Independent of pressure levels

As for the carbon monoxide (CO) data, they come from the EAC4 (ECMWF *Atmospheric Composition Reanalysis* 4; https://atmosphere.copernicus.eu) [19]. They are extracted at a resolution of 0.75˚ × 0.75˚, at a time resolution of 3 *hours* and over several atmospheric pressure levels.

2.3. Methods

The modeling of pollutant dispersion in our area is carried out through the combined application of two methods. The first methodological approach consists of developing a mathematical model that represents the dynamics of pollutant dispersion. The second step involves calibrating the analytical model, which is derived from the mathematical model.

2.3.1. Mathematical Formulation

In the context of this study, we consider $\mathbb{Q}$ as the theoretical domain of study of the model such that:

$$\begin{cases} \Omega = \left\{\mathbb{R}, \mathbb{R}, \mathbb{R}^{+}\right\}, \\ (x, y, z, t) \in \mathbb{Q} = \Omega \times [0, T[, \\ (x, y, z, 0) \in \mathbb{Q}_0 = \Omega \times \{0\}, \\ \Lambda = \partial\Omega \times [0, T[. \end{cases} \tag{1}$$

The dynamics of pollutant dispersion are governed by the equation:

$$\begin{aligned} &\frac{\partial}{\partial t}\left(K_x \frac{\partial c}{\partial x}\right) + \frac{\partial}{\partial t}\left(K_y \frac{\partial c}{\partial y}\right) + \frac{\partial}{\partial t}\left(K_z \frac{\partial c}{\partial z}\right) - V_x \frac{\partial}{\partial x}\left(K_x \frac{\partial c}{\partial x}\right) \\ &- V_y \frac{\partial}{\partial y}\left(K_y \frac{\partial c}{\partial y}\right) - V_z \frac{\partial}{\partial z}\left(K_z \frac{\partial c}{\partial z}\right) \\ &= -\left(\sigma_u^2 \frac{\partial c}{\partial x}\right) - \left(\sigma_v^2 \frac{\partial c}{\partial y}\right) - \left(\sigma_w^2 \frac{\partial c}{\partial z}\right) + \frac{\partial}{\partial x}\left[\sigma_u \wedge_x \frac{\partial}{\partial x}\left(K_x \frac{\partial c}{\partial x}\right)\right] \\ &+ \frac{\partial}{\partial y}\left[\sigma_v \wedge_y \frac{\partial}{\partial y}\left(K_y \frac{\partial c}{\partial y}\right)\right] + \frac{\partial}{\partial z}\left[\sigma_w \wedge_z \frac{\partial}{\partial z}\left(K_z \frac{\partial c}{\partial z}\right)\right], \end{aligned} \tag{2}$$

where c is the pollutant concentration; V_x, V_y and V_z are the components of the wind speed vector u; σ_u, σ_v and σ_w are the standard deviations (or the variances of the along-wind and horizontal and vertical accross-wind speed respectively) of turbulent velocity fluctuation in the x, y and z directions, respectively. K_x, K_y and K_z are a diffusivity coefficient (in units of m²/sec); $\wedge_x$, $\wedge_y$ and $\wedge_z$ corresponds to the diffusion scale which is a macroscopic scale [26]. The main Equation (2) is derived from the transport equation for turbulent scalar fluxes [17]. This equation includes first- and second-order tensors. Closing the first-order tensors yields the diffusion coefficients [27]. Similarly, closing the second-order tensors yields the velocity standard deviations and diffusion scales [27]. We assume the following assumptions:

1) The diffusion coefficients, velocity coefficients, and diffusion scales are constant;

2) At $t_0 = 0$ s

$$c(x,y,z,t_0) = f(x,y,z) \quad \forall (x,y,z) \in \{\mathbb{R},\mathbb{R},\mathbb{R}^+\}; \tag{3}$$

3) For any from the source, the concentration decreases to zero, i.e:

$$\forall\, x,y,z \text{ if } t \to T \text{ then } c \to 0; \tag{4}$$

4) The pollutant is not absorbed by the soil surface:

$$-K_z \frac{\partial c}{\partial z} = 0 \text{ at } z = 0; \tag{5}$$

5) We assume pollutant emissions from a point source located at $(0,0,H)$; where $f(x,y,z) = q\delta(x)\delta(y)\delta(z-H)$; q is the emission rate and δ the *Dirac's* delta function. So, the mathematical model of pollutant dispersion is presented by the following system:

$$\Upsilon = \begin{cases} K\dfrac{\partial}{\partial t}(\nabla c) + A\Delta c - \sigma^2 \nabla c + B\nabla \Delta c = 0 & \text{in } \mathbb{Q}, \\ c(x,y,z,0) = f(x,y,z) & \text{in } \mathbb{Q}_0, \\ K_z \dfrac{\partial c}{\partial z} = 0 & \text{at } z = 0, \\ c \to 0 \quad \forall x,y,z & \text{if } t \to T, \\ (x_0,y_0,z_0) = (0,0,z_0) & \text{if } t = 0, \end{cases} \tag{6}$$

where $K = \begin{pmatrix} K_x & 0 & 0 \\ 0 & K_y & 0 \\ 0 & 0 & K_z \end{pmatrix}$; $A = \begin{pmatrix} A_x & 0 & 0 \\ 0 & A_y & 0 \\ 0 & 0 & A_z \end{pmatrix}$; $B = \begin{pmatrix} B_x & 0 & 0 \\ 0 & B_y & 0 \\ 0 & 0 & B_z \end{pmatrix}$;

$\sigma^2 = \begin{pmatrix} \sigma_u^2 & 0 & 0 \\ 0 & \sigma_v^2 & 0 \\ 0 & 0 & \sigma_w^2 \end{pmatrix}$ and $A_i = K_i V_i$, $B_i = \sigma_\alpha \wedge_i K_i \quad \forall i \in \{x,y,z\}$ and $\alpha \in \{U,V,W\}$ respectively.

The objective of the mathematical model is to ascertain a solution for the concentration of pollutants, with a view to controlling their dispersion and distribution in the $\mathbb{Q}$ domain. Solving this system (6) of equations directly proves to be a significant challenge due to the inherent complexities of this type of mathematical model. In our study, we opted for a variational methodology to verify the existence and uniqueness of a solution to the system. This approach will also allow us to determine the optimality conditions, enabling us to find an optimal solution.

Let $\mathcal{J}$ be a function denoted by: $\mathcal{J}$ defined by:

$$\mathcal{J} : (c,c_0) \mapsto \mathcal{J}(c,c_0) = \int_{\mathbb{Q}=\Omega\times(0,T)} L(c(t),c_0)\,\mathrm{d}x\mathrm{d}y\mathrm{d}z\mathrm{d}t, \tag{7}$$

$$c \in V_{ad} = \{c \in L^\infty(\mathbb{Q}) : c_a \le c \le c_b\},$$

where c_0 (initial concentration): the control; c (instantaneous concentration): the state variable; V_{ad}: the control domain; L is the Lagrangian function that meets the following criteria:

- $L : \mathbb{Q} \to \mathbb{R}$ is caratheodory function;

- $\forall(x,y,z,t)\in\mathbb{Q}$, $L(c,c_0)$ is of class $C^2\in\mathbb{R}^2$;
- $\forall(x,y,z,t)\in\mathbb{Q}$, $L(c,c_0)$ is convex on the set in V_{ad}.

The problem posed is therefore to minimize this functional $\mathcal{J}(c,c_0)$ under the system (6) constraint when $c_0\in V_{ad}$. This is a major constraint of the problem posed. A weak formulation of the problem is formulated by minimizing a new functional $\mathcal{A}$ dependent on $\mathcal{J}(c,c_0)$.

Let $\mathcal{A}$:

$$\mathcal{A}(c,c_0;p)=\mathcal{J}(c,c_0)+\int_{\mathbb{Q}}\mathcal{M}(c,c_0)\cdot p\mathrm{d}w \tag{8}$$

$$\mathcal{A}(c,c_0;p)=\int_{\mathbb{Q}=\Omega\times(0,T)}L(c(t),c_0)\mathrm{d}w+\int_{\mathbb{Q}=\Omega\times(0,T)}\mathcal{M}(c,c_0)\cdot p\mathrm{d}w, \tag{9}$$

with $p\in\left[C_0^2(\mathbb{Q})\right]^3$ the adjointe variable and we denote $\mathrm{d}x\mathrm{d}y\mathrm{d}z\mathrm{d}t=\mathrm{d}w$. The function $\mathcal{M}(c,c_0)$ represents the function associated with the variational equation of the evolution equation of the mathematical model of pollutant dispersion.

Furthermore, optimized functionality $\mathcal{J}$ returns to optimized $\mathcal{A}$:

$$\min_{c;c_0\in V_{ad}}\mathcal{J}(c,c_0)=\min_{c;c_0}\max_{p}\mathcal{A}(c,c_0,p) \tag{10}$$

Existence and uniqueness

In this session, we use monotone operator theory [22] to demonstrate the existence and uniqueness of a solution to the problem at hand. Operator theory is a powerful tool used in optimization.

In the theoretical study of the model, matrices A, K, σ^2 and B are considered constants.

We consider the evolution equation:

$$K\frac{\mathrm{d}}{\mathrm{d}t}(\nabla c)+A\Delta c-\sigma^2\nabla c+B\nabla\Delta c=0 \text{ in } \mathbb{Q}. \tag{11}$$

Let $\mathcal{L}$ the operator associated of the equation (11) such that:

$$\mathcal{L}(.)=K\frac{\mathrm{d}}{\mathrm{d}t}\left[\nabla(.)\right]+A\Delta(.)-\sigma^2\nabla(.)+B\nabla\Delta(.) \tag{12}$$

and

$$\begin{aligned}\mathcal{D}(\mathcal{L})=\Big\{&\varsigma\in H_0^1:\mathcal{L}(\varsigma)=K\frac{\mathrm{d}}{\mathrm{d}t}\left[\nabla(\varsigma)\right]+A\Delta(\varsigma)-\sigma^2\nabla(\varsigma)\\&+B\nabla\Delta(\varsigma);\ \varsigma(x,y,z,0)=\varsigma_0\ \ K_z\frac{\partial\varsigma}{\partial z}=0 \text{ if } z=0;\\&\text{and } \varsigma(x,y,z,\infty)=0\ \ \forall(x,y,z)\in\Omega\Big\}.\end{aligned} \tag{13}$$

Let c_1 and c_2, two molarities of the same pollutant. Let's calculate the *dot product* in *Sobolev space* [20]:

$$\begin{aligned}&\left\langle\mathcal{L}(c_1)-\mathcal{L}(c_2),(c_1-c_2)\right\rangle\\&=K\int_{\mathbb{Q}}\frac{\mathrm{d}}{\mathrm{d}t}\left[\nabla(c_1-c_2)\right](c_1-c_2)\mathrm{d}w+A\int_{\mathbb{Q}}\left[\Delta(c_1-c_2)\right](c_1-c_2)\mathrm{d}w\\&\quad-\sigma^2\int_{\mathbb{Q}}\left[\nabla(c_1-c_2)\right](c_1-c_2)\mathrm{d}w+B\int_{\mathbb{Q}}\left[\nabla\Delta(c_1-c_2)\right](c_1-c_2)\mathrm{d}w.\end{aligned} \tag{14}$$

Once the calculation and minimization **(proof of the calculation and minimization can be found in Appendix A)** of this quantity $\langle \mathcal{L}(c_1)-\mathcal{L}(c_2),(c_1-c_2)\rangle$ have been carried out, we obtain the following relationship:

$$\langle \mathcal{L}(c_1)-\mathcal{L}(c_2),(c_1-c_2)\rangle \geq \lambda' \|c_1-c_2\|^2, \tag{15}$$

with $\lambda' = constant$. So the operator $\mathcal{L}$ is *strongly monotone*.

Let c_0 and c be two different concentrations:

$$\begin{aligned}\mathcal{L}(c)-\mathcal{L}(c_0) = K\int_{\mathbb{Q}} \frac{\mathrm{d}}{\mathrm{d}t}\left[\nabla(c-c_0)\right]\mathrm{d}w + A\int_{\mathbb{Q}}\left[\Delta(c-c_0)\right]\mathrm{d}w \\ -\sigma^2\int_{\mathbb{Q}}\left[\nabla(c_1-c_2)\right]\mathrm{d}w + B\int_{\mathbb{Q}}\left[\nabla\Delta(c-c_0)\right]\mathrm{d}w.\end{aligned} \tag{16}$$

If $c \to c_0$ therefore $\left(\mathcal{L}(c)-\mathcal{L}(c_0)\right)\to 0$.

This operator is continue. Thus, the problem (10) has a unique solution.

Optimality systems

We determine the variation of the Lagrange functional and apply the principle of least actions to it in order to find the optimality condition.

Let's δc and δc_0 be small variations of c and c_0 ($c, c_0 \in H(Q)$); with $L_c = \dfrac{\partial L}{\partial c}$ and $L_{c_0} = \dfrac{\partial L}{\partial c_0}$.

The variation of Lagrange functional is:

$$\begin{aligned}\Delta\mathcal{A} = \int_{\mathbb{Q}}\left[L_c(c,c_0) - K\nabla\frac{\partial p}{\partial t} + A\Delta p + \sigma^2\nabla p + B\Delta(\nabla p)\right]\delta c\,\mathrm{d}w \\ + o\left(\sqrt{(\delta c)^2 + (\delta c_0)^2}\right) + \int_{\Omega}\left[\int_0^T L_{c_0}(c,c_0)\,\mathrm{d}t + K\nabla p(0)\right]\delta c_0\,\mathrm{d}\Omega\end{aligned} \tag{17}$$

Proof: See **Appendix B** for details.

Based on the principles of least action and setting the derivative of the Lagrangian with respect to the variables c and c_0 equal to 0, we obtain the following optimality system:

- **direct model**

$$\begin{cases} K\dfrac{\partial}{\partial t}(\nabla c) + A\Delta c - \sigma^2\nabla c + B\nabla\Delta c = 0 & \text{in } \mathbb{Q}, \\ c(x,y,z,0) = f(x,y,z) & \text{in } \mathbb{Q}_0, \\ K_z\dfrac{\partial c}{\partial z} = 0 & \text{at } z=0, \\ c \to 0 \quad \forall x,y,z & \text{if } t \to \pm\infty, \\ (x_0,y_0,z_0) = (0,0,H) & \text{if } t=0, \end{cases} \tag{18}$$

- **adjoint model**

$$K\nabla\frac{\partial p}{\partial t} - A\Delta p - \sigma^2\nabla p - B\Delta(\nabla p) = 0,\ \ p(T) = 0, \tag{19}$$

- **optimality condition**

$$K\nabla p(0) = 0. \tag{20}$$

Analysis of the resulting optimality system leads to the conclusion that an op-

timal solution exists that minimizes the functional (10). In this study, an analytical solution to the mathematical model will be obtained through the Fourier transform. The analytical (see **Appendix C** for details) approach is:

$$c(x,y,z,t)=\frac{q}{8\bar{u}(\pi t)^{3/2}}\times\sqrt{\frac{K_xK_yK_z}{B_xB_yB_z}}\times\exp\left[\frac{\left(xK_x+A_xt+\sigma_u^2t\right)^2}{\left(4B_xt\right)}+\frac{\left(yK_y+A_yt+\sigma_v^2t\right)^2}{\left(4B_yt\right)}+\frac{\left(K_z(z)+A_zt+\sigma_w^2t\right)^2}{4B_zt}\right]. \tag{21}$$

2.3.2. Validation of the Model

Parametrization of diffusion coefficients

The implementation of this analytical solution (21) requires the parameterization of diffusion coefficients and standard deviations of velocities. This parameterization depends on the type of stability exhibited by the atmosphere in which the dynamics of the pollutant are studied. There are three types of atmospheric stability: a neutral atmosphere, a stable atmosphere, and an unstable atmosphere. This stability depends on the velocity, the vertical temperature gradient, which in turn depends on the sunshine (day) and the cloud cover (night). Stability is a complex phenomenon of turbulence. Turbulence is represented by a class that allows parameterization of the diffusion standard deviations [28].

BATCHELOR (1949) [29], proposes a parameterization of the diffusion coefficients according to the standard deviations of the concentrations, which results in the following relationships:

$$K_\alpha=\frac{\bar{u}}{2x}\sigma_\alpha^2, \tag{22}$$

with $\alpha=\{x,y,z\}$, where $\bar{u}$ mean-wind speed; x is downwind distance and σ_α is standard deviation or dispersion parameter in the αth direction. For stable, unstable or neutral conditions, the expression for σ_x and σ_y are (*CIRILLIO and POLI* 1992) [30]:

$$\sigma_x=x\left[\cosh\left(\sigma_\theta^2\right)-1\right]^{-1/2}, \tag{23}$$

$$\sigma_y=x\left[\sinh\left(\sigma_\theta^2\right)\right]^{-1/2}, \tag{24}$$

where σ_θ is the horizontal direction of the wind. The variable σ_z is parameterized according to the Pasquill-Turner classification table [31]. The diffusion coefficients, K_x and K_y, vary depending on wind speed and horizontal direction, as well as space. Wind speed is a time-dependent variable. Therefore, these coefficients vary over time. The diffusion coefficient K_z varies depending on atmospheric stability and space.

The standard deviations of the velocities are expressed using the following formulas:

- for unstable condition:

$$\left(\frac{\sigma_u}{\overline{u}}\right)^2 = \left(\frac{\sigma_v}{\overline{u}}\right)^2 = 0.36\left(w_*/\overline{u}\right)^2, \tag{25}$$

$$\left(\frac{\sigma_w}{\overline{u}}\right)^2 = 0.16\left(w_*/\overline{u}\right)^2, \tag{26}$$

- for stable condition:

$$\left(\frac{\sigma_u}{\overline{u}}\right)^2 = 6.25\left(u_*/\overline{u}\right)^2, \tag{27}$$

$$\left(\frac{\sigma_v}{\overline{u}}\right)^2 = 3.61\left(u_*/\overline{u}\right)^2, \tag{28}$$

$$\left(\frac{\sigma_w}{\overline{u}}\right)^2 = 1.69\left(u_*/\overline{u}\right)^2, \tag{29}$$

where u_* is friction velocity and w_* convective velocity. Turbulence intensities depend on average wind speed, convection, friction velocity, and atmospheric stability. Average wind speed, convection, and friction velocity vary over time. Therefore, these intensities vary over time. The necessary and sufficient condition of these empirical relationships is the hypothesis of weak winds in the lower troposphere (atmospheric boundary layer) [32]. Weak winds are observed almost everywhere precisely in the atmospheric boundary layer. Tropical areas are the most exposed to weak winds which promote the diffusion of pollutants [33].

Assimilation data (4D-Var)

A model, however efficient, is not sufficient on its own to make a prediction: it is essential to provide an initial condition deduced from the dynamic observation of the flow [34]. It is essential that this initial condition be as close as possible to the observations while remaining compatible with the model. There are two methods for determining this initial condition: optimal interpolation (OI), which is a statistical method, and the variational method. Optimal interpolation encountered difficulties in the 1980s, notably due to its inability to dynamically handle uncertainties in forecasting, its difficulty in determining initial conditions, and its failure to adequately integrate satellite data [35]. The variational approach 4D-Var (from control theory [36]) formulates data assimilation as a nonlinear optimization problem constrained by a numerical model [37]. Its objective is to take into account recent atmospheric observations in order to readjust the trajectory of a numerical weather prediction model [38]. This approach involves minimizing a functional using the adjoint method in order to find its gradient (*Lions* 1968 [39]). It found its application in meteorology for the first time by *Le Dimet and Talagrand* (1986) [40], to one-dimensional models, to filtered models (*Lewis et al.* 1985) [41]; (Derber 1987) [42], and shallow water equations (*Courtier and Talagrand* 1990) [43].

However, we use this technique to calibrate our model and determine initial concentrations, which will serve as reference data for forecasts. Thus, the pollutant concentration is evaluated according to time, pressure level, and within each sub-

grid (cell) of the domain $\mathbb{Q}$, using the analytical formula (21).

Let $C_0 = \{c_{0_1}, \cdots, c_{0_N}\}$ be the set of initial concentrations evaluated at an altitude and C_k the one evaluated at t_k. Let:

$$C_k = \mathcal{I}_{t_0 \to t_k}(C_0) \text{ with } C_k \in \mathbb{R}^{d_x};\ k = 1, \cdots, N \tag{30}$$

where $\mathcal{I} : \mathbb{R}^{d_x} \times \mathbb{R}^{d_x}$ represents the model describing the evolution of the concentration from t_0 to t_k.

$$d_x = n_t \times n_{level} \times n_{lat} \times n_{lon} \tag{31}$$

$$d_x = 8 \times 5 \times 88 \times 121$$

$$d_x = 425920, \tag{32}$$

$n_t = 8$ is the number of hour steps in a day; $n_{level} = 5$ is the number of pressure levels; $n_{lat} = 88$ and $n_{lon} = 121$ are the dimensions of the domain where the cells of dimensions are 28 km × 28 km. Let:

$$\mathcal{H} : \mathbb{R}^{d_x} \to \mathbb{R}^{d_y}, \tag{33}$$

be the observation operator that links the estimated state of the model to the observation corresponding to each instant t_k with $k = 1, \cdots, N$ and $d_y = 5 \times 8 \times 30 \times 41 = 49200$. In mathematical modeling, the observation operator $\mathcal{H}$ maps the complete state vector of the *four-dimensional* model (*time × pressure levels × latitude × longitude*) into the observation space. This representation is achieved through a linear projection. The model state is first vectorized into a one-dimensional array: $C_k \in \mathbb{R}^{d_x}$. The operator $\mathcal{H}$ is structured as a sparse linear selection matrix, whose function is to extract only the state components corresponding to the available satellite observations. More specifically, a Boolean observation mask is used to identify the observed grid points and pressure levels. The operator, by its linearity, is a function of time, as demonstrated by the observation mask, which reflects the spatial and temporal availability of satellite retrievals.

The observation vector y_k^0 at time t_k and the noise vector ν_k are defined by the following application:

$$y_k^0 = \mathcal{H}(C_k) + \nu_k, \tag{34}$$

with $y_k^0 \in \mathbb{R}^{d_y}$; $\nu_k \sim \mathcal{N}(\sigma^2, \mathcal{R}_k)$ and $\sigma^2 = 0.01^2$ [24] [37]. The observation error (ν_k) is unbiased, uncorrelated in time. The observation vector (y_k^0) corresponds to satellite images of carbon monoxide (CO) concentration at a time t_k. The functional associated with the variational approach is [44]:

$$\begin{aligned} \mathbb{S}(C_0) = &\frac{1}{2}\sum_{k=0}^{N}\left[y_k^0 - \mathcal{H}(C_k)\right]^{\mathrm{T}} R_k^{-1}\left[y_k^0 - \mathcal{H}(C_k)\right] \\ &+ \frac{1}{2}\left[C_0 - C_b\right]^{\mathrm{T}} \mathcal{F}_0^{-1}\left[C_0 - C_b\right], \end{aligned} \tag{35}$$

with

- $C_b \sim \mathcal{N}(0.04, \mathcal{F}_0)$ is the initial background state [24];
- $R_k = 0.01^2 I_{dy} \in \mathbb{R}^{d_y \times d_y}$ is the error covariance diagonal matrix of the obser-

vation [24] [37];

- $\mathcal{F}_0 = 0.04 I_{d_x} \in \mathbb{R}^{d_x \times d_x}$ the model error covariance diagonal matrix [37], with I_{d_x} the identity matrix.

The problem of data assimilation using the 4D-Var method is therefore:

$$(\mathcal{IV}): \begin{cases} C_k = \mathcal{I}_{t_0 \to t_k}\left(\hat{C}_0\right) & C_k \in \mathbb{R}^{d_x}, \\ y_k^0 = \mathcal{H}\left(C_k\right) + \nu_k & y_k^0 \in \mathbb{R}^{d_y}, \\ C(0) = C_0 & C_0 \in \mathbb{R}^{d_x}, \\ \hat{C}_0 = \arg\min\limits_{C_0 \in \mathbb{R}^{d_x}} \mathcal{S}\left(C_0\right) & \hat{C}_0 \in \mathbb{R}^{d_x}. \end{cases} \tag{36}$$

The control vector consists of the complete four-dimensional concentration field defined over all time steps of the assimilation window, all pressure levels, and all horizontal grid points. The algorithm of choice for minimisation is the *Quasi-Newton limited memory L-BFGS* algorithm as devised in (*Nocedal* 1980) [45] and (*Liu and Nocedal* 1989) [46]. The 4D-Var assimilation window spans a period of three hours (03 h), corresponding to the complete integration period of the direct model. The model is integrated continuously over this fixed window. Consequently, all satellite observations available during this period are assimilated simultaneously at their respective acquisition times. The 4D-Var cost function is minimized by the quasi-Newton L-BFGS algorithm with an analytically derived adjoint gradient. It should be noted that the number of iterations is limited to 100 ($maxiter = 100$), and that the default stopping criteria of the SciPy implementation are applied (projected gradient norm and relative cost reduction). The corresponding inverse covariance matrices weight the observation and background terms of the cost function and ensure regularization of the problem. The dynamic system consists of nine (09) input data points. These include eight (8) *ERA*5 meteorological variables, as well as carbon monoxide concentration images. The data are daily with a three-hourly interval. The model makes eight (08) estimates per day based on altitude. Due to the considerable size of the data, the numerical simulations require the use of a powerful and suitable computer, given the complexity of the necessary mathematical calculations. Due to the size of the available data, the simulations were performed on a calculator. To evaluate the robustness of the model, we use the Root Mean Square Error (*RMSE*) metric [24], the fractional bias (*FB*) [23], and the fraction of predictions within a factor of two of the observations (*FAC*2) [23]:

$$RMSE = \sqrt{\frac{1}{M} \cdot \sum_{k=0}^{M} \left(\hat{c}_{0_k} - y_k^0\right)^{\mathrm{T}} \cdot \left(\hat{c}_{0_k} - y_k^0\right)}, \tag{37}$$

$$FB = \frac{\overline{y_k^0} - \overline{\hat{c}_{0_k}}}{0.5\left(\overline{y_k^0} + \overline{\hat{c}_{0_k}}\right)}, \tag{38}$$

$$FAC2 = \frac{\hat{c}_{0_k}}{y_k^0}, \tag{39}$$

where $\bar{C}$ represents the average over the dataset and $\hat{c}_{0_k}$ the estimated initial concentration at time t_k.

3. Results and Discussion

In this session, we present the results of the implementation of the model coupled with the variational approach (4D-Var), which is divided into two parts. First, we compare the output maps of the coupled model with the observations incorporated into it. The second part of this study focuses on the analysis of the output maps of the coupled system. It should be noted that the experiments were conducted using data from the dry season (December-January-February), specifically December 1st, 2023. The dry season is characterized by lower humidity and higher than normal temperatures along the West African coast. The prevailing wind during this season carries many particles from the Sahara Desert southward. This is a period during which high levels of carbon monoxide (CO) accumulate in the Gulf of Guinea [13] [47]. The weather conditions on the chosen day are determined by solar radiation during the day and cloud cover at night, according to the Pasquill-Turner classification table [31].

3.1. Algorithm Workflow: Coupled System Algorithm Model-4D-Var

Figure 2 shows satellite images (left) and dispersion maps (right) from the Model-4D-Var coupling system. These dispersion maps illustrate the evolution of dispersion and the estimated concentration of carbon monoxide at 1000 hPa, 950 hPa, and 850 hPa as a function of time. We observe that the dispersion maps of the coupling system (right-hand images) are smoother and allow for the quantification of CO pollutant plumes. Furthermore, these maps enable us to track the spatio-temporal trajectories of the plumes with greater precision. They contribute to a better understanding of pollutant transport at different meteorological scales in the Gulf of Guinea. This is due to the integration of the 4D-Var data assimilation technique, a major strength of the system. This technique allows it to produce better estimates consistent with satellite observations and to reduce uncertainties compared to available emission inventories, which are sometimes biased in West Africa. This performance is close to modern techniques based on the automation of quantification and detection of plumes of pollutants (CH_4) recently developed [48]-[52]. These machine learning techniques use satellite and hyperspectral images (Sentinel-2, PRISMA, EnMAP, EMIT and CarbonMapper) to detect plumes and estimate concentrations of pollutants from combustion and industries etc.

Obtaining carbon monoxide dispersion maps with a resolution scale of ($0.25^\circ \times 0.25^\circ$) compared to satellite images with a resolution of $0.75^\circ \times 0.75^\circ$ is part of one of the model's performances. The concentration in each grid cell is estimated using the analytical formula (21). This formula takes into account the horizontal

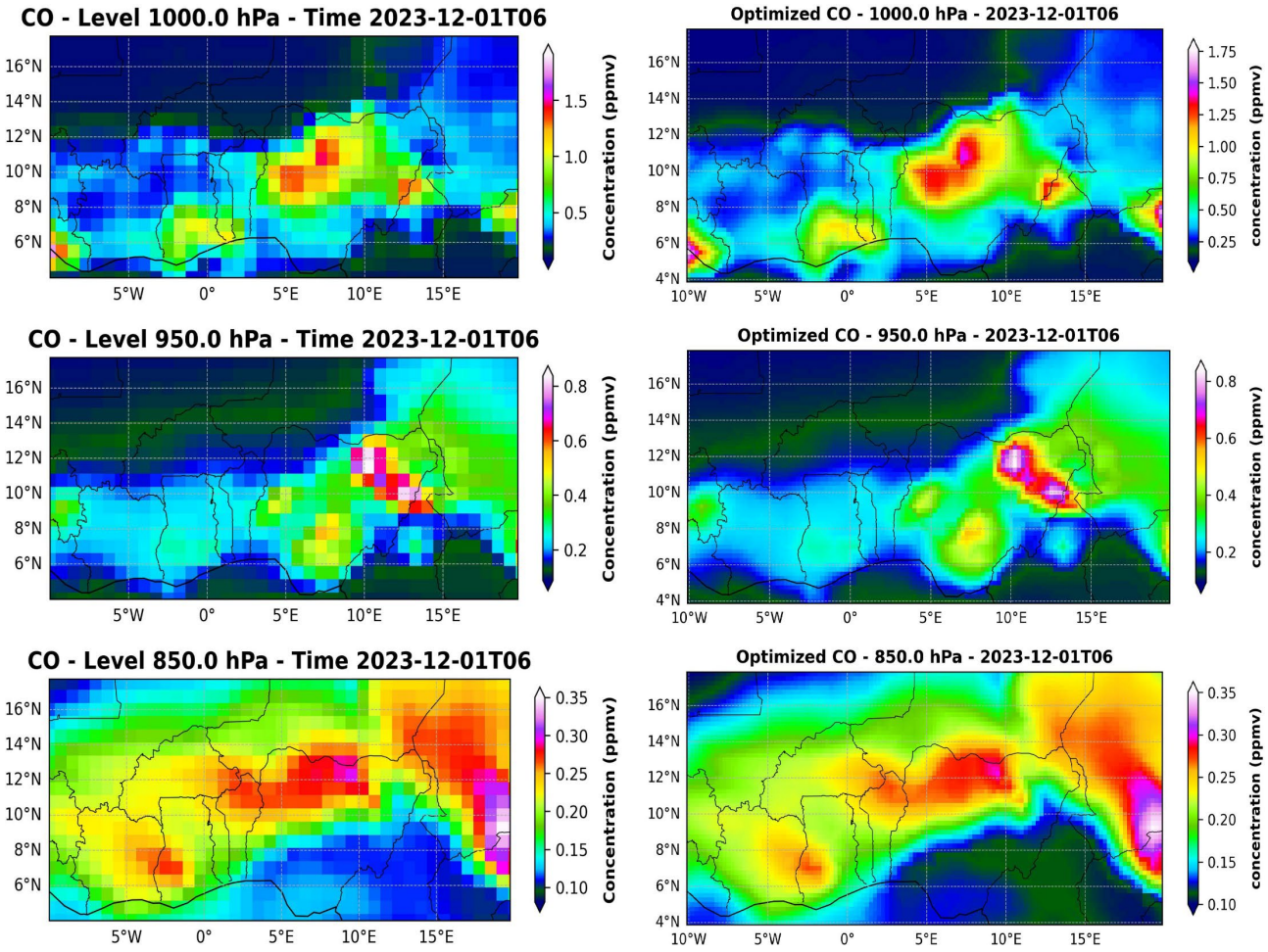

Figure 2. Satellite images are on the left and those generated by the model are on the right at 1000 hPa, 950 hPa 850 hPa depending on the time.

and vertical distribution of carbon monoxide as a function of pressure levels. It considers advection, diffusion, convection, atmospheric stability (clouds, solar radiation), and turbulence through parameterizations of the diffusion coefficients $\left(k_x, K_y, K_z\right)$ and velocity standard deviations $(\sigma_u, \sigma_v, \sigma_w)$.

The low values of the mean squared error (**Figure 3**), attest that the results of the model are close to the observations. This property also demonstrates the system's effectiveness and its ability to generate dispersion maps that accurately reflect real-world observations. The system reproduces carbon monoxide dispersion more accurately than observations. Indeed, at 1000 hPa these values are considered high compared to other pressure levels, namely (950 hPa; 900 hPa; 850; 800 hPa) between 00 h - 06 h. The results obtained are inconsistent with observations recorded at this pressure level 1000 hPa. The anomaly observed at 1000 hPa is related to the choice of parameters for the diffusion coefficients and velocity standard deviations. At this level, the appropriate parameters for the diffusion coefficients are those of Monin and Obukhov [53]. Those suitable for the velocity standard deviations are those proposed by Irwin (1970) and Wyngaard *et al.* (1974-1975), as reported by Hanna *et al.* [27].

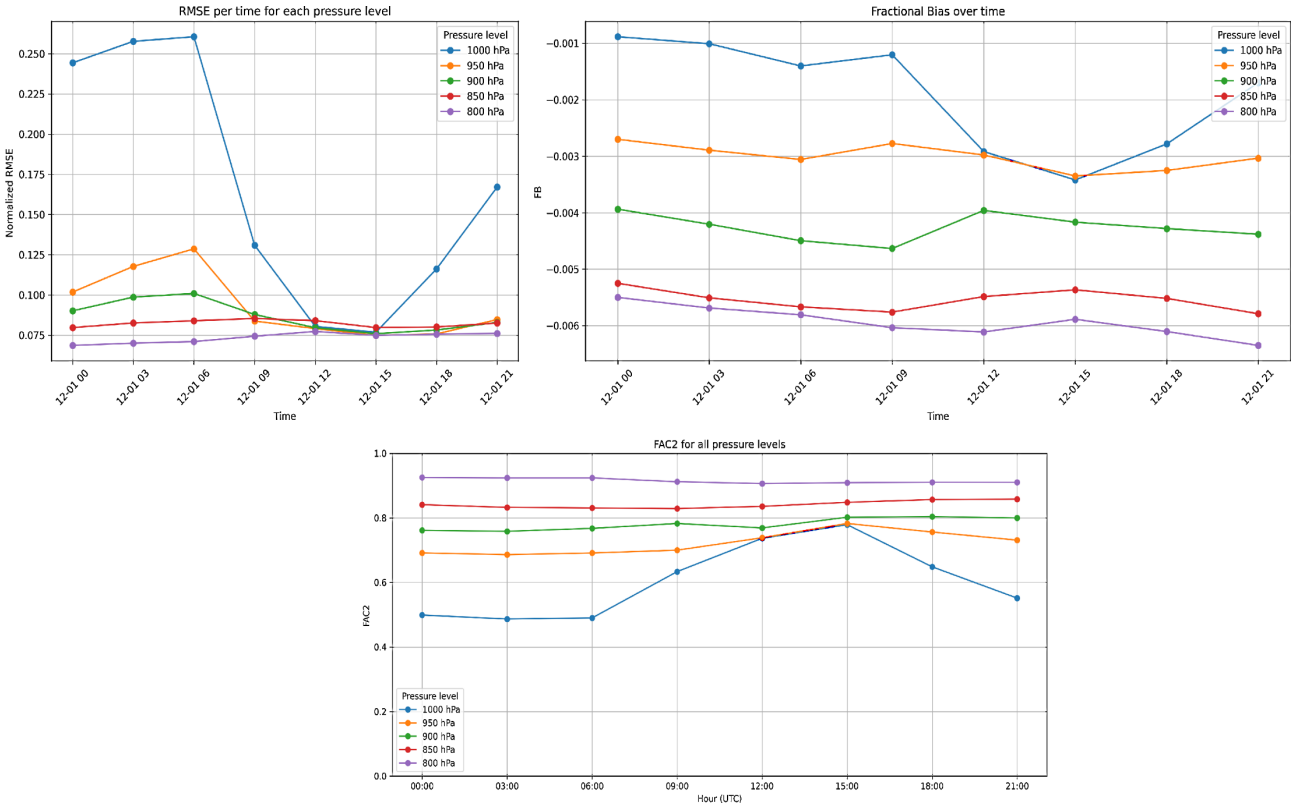

Figure 3. RMSE, fractional bias and FAC2 of the model.

However, the objective of our study is to investigate the dispersion of pollutants at pressure levels above 1000 hPa; therefore, we cannot use these formulations, which could introduce physical inconsistencies into the model. It should be noted, however, that this anomaly does not significantly affect the overall performance of the model when the pressure level is above 1000 hPa. The fractional bias (*FB*) values obtained at each pressure level were found to be very low and negative ($FB < 0$). The negative sign ($FB < 0 \Rightarrow \overline{y_k^0} < \overline{c_{0_k}}$) indicates that the model overestimates carbon monoxide concentration values. However, the results obtained indicate that the overestimates is negligible compared to the actual values from satellite images. This study shows that the model estimates correlate perfectly with satellite images.

When analyzing the data (**Table A1**), it is essential to specify that the fraction data (*FAC*2) values, determined for each pressure level (**Figure 3**), are between 0.5 and 2. These values comply with current standards and reflect the model's good performance ($0.5 \le FAC2 \le 2$) in terms of reproducing the pollutant dispersion process. In addition, it has been found that the model's performance is limited to 1000 hPa between midnight and 6 a.m. This observation confirms the anomaly identified by the *RMSE* at this constant pressure level.

3.2. Analysis of the Dispersion Output Maps of the Model-4D-Var

The 1000 hPa dispersion maps (**Figure 4**) show carbon monoxide concentration

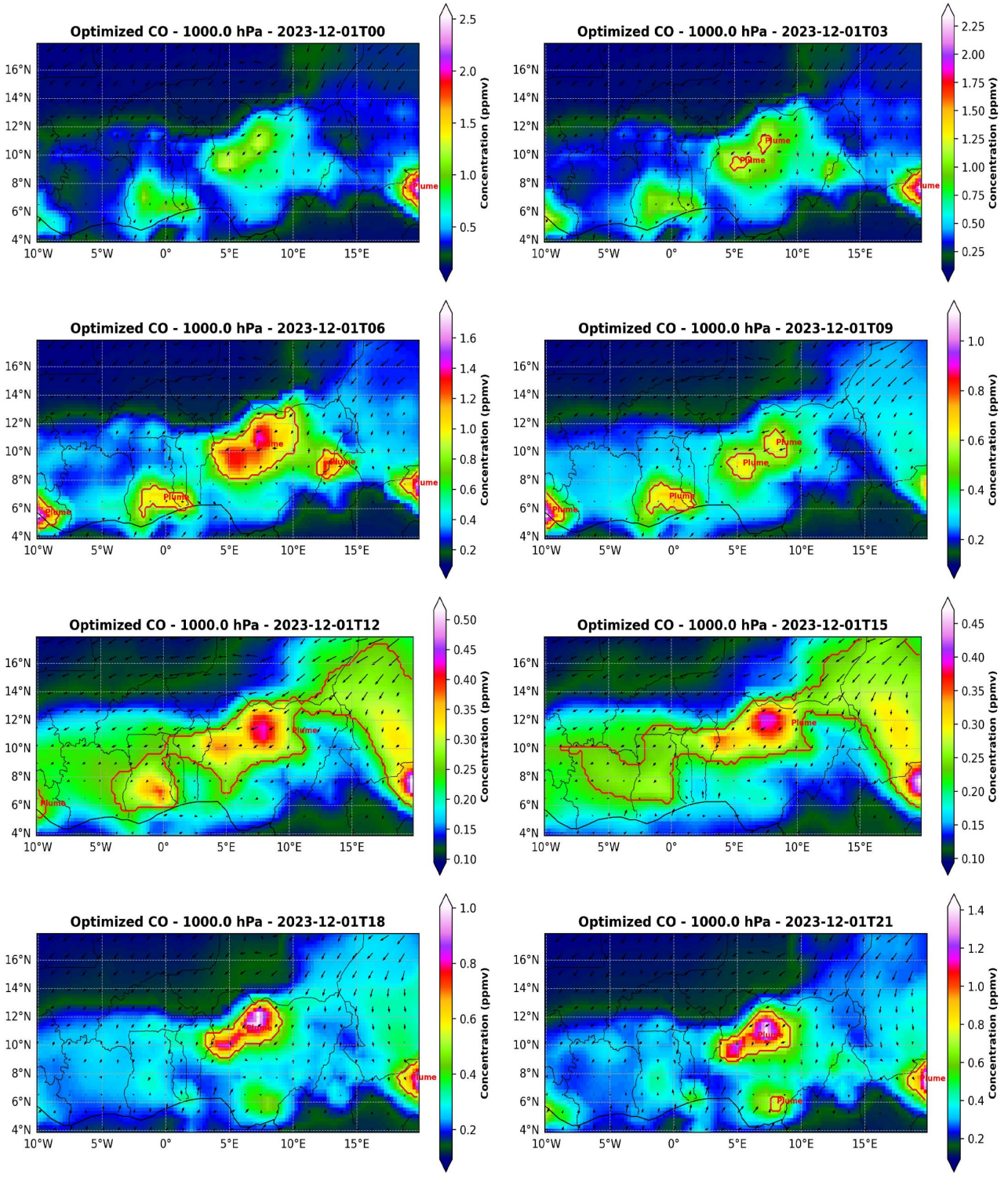

Figure 4. Temporal evolution of carbon monoxide concentration at 1000 hPa.

values ranging from 2.5 ppmv to 1.4 ppmv (in practice 1 ppmv = 1 ppm), with a resolution of three hours. According to the World Health Organization (WHO), the recommended atmospheric concentration threshold is 7 mg/m^3 (approxi-

mately 6.1 ppm at 25˚C) for a 24 h exposure period [54]. Further research has established a correlation between exposure to ambient carbon dioxide concentrations below 1 ppm (approximately 1.15 mg/m^3 at 25˚C) over a period of one hour and an increased risk of cardiovascular disease [55] [56]. This observation contradicts the guidelines established by the World Health Organization (WHO). *Chen et al.* (2021) [57] conducted studies using data from 1979 to 2016, covering 337 cities in 18 countries. This research highlights the absence of a threshold concentration for CO, suggesting instead a correlation between the risk of cardiovascular disease or daily mortality and a 1 mg/m^3 (approximately 0.87 ppm at 25˚C) increase in this gas. In their study, *Samoli et al.* (2007) [58] demonstrated the existence of significant co-mortality risks for concentrations below 0.5 mg/m^3 (approximately 0.44 ppm at 25˚C), in the case of maximum average exposure over an 8 h period.

These results show that, for exposure lasting one hour (1 h) and a threshold value of 1 ppmv, the risk of cardiovascular disease is proven. Furthermore, for a period of three hours, the value must be below 1 ppmv. Polluted areas are therefore territories in which carbon monoxide concentrations exceed the threshold of 1 ppmv. In these areas, populations are exposed to levels of carbon monoxide (CO) that can have harmful effects on health, including respiratory diseases and even death. It has been found that most of these areas are those where continuous emissions of pollutants occur. These emissions are characterized by their spread over altitude and increased persistence on a satellite scale.

3.2.1. Quantification of Local Plumes

- At 1000 hPa (**Figure 5**) and at 06 h, we detect a local plume that appears in *Liberia* in the region of 5.5˚N and 10˚W with a concentration of approximately to 2.25 ppmv. This plume disperses slowly under the influence of a light southerly wind, and disappears around 12 h. It has little impact on the area during this period.
- At 950 hPa (**Figure 6**), a second plume is located south of *Nigeria* at around 7˚E and 6˚N. It is present at 00 h with a maximum concentration of approximately 1.6 ppmv, which decreases over time (00 h; 03 h; 06 h), but rises again around 18 h with a value close to 0.45 ppmv.

The dispersal of this plume is primarily influenced by the monsoon (south wind) due to its location near the Atlantic Ocean. This south wind, observed in the southern coastal regions, blows between 00 h and 06 h, and ceasing when the harmattan becomes dominant. Before 06 h, we note a sunrise with a less cloudy sky (**Figure 7**) marking the dispersion of the plume. During the sunny day, the sky is clear and the daytime heating becomes significant. This marks the presence of the sea breeze which promotes a rapid dispersion of the plume with a decrease in concentration, or even cancellation between 12 h - 03 h (**Figure 6**). Clouds reappear after 06 h, the atmosphere becomes stable, and dispersion is limited, leading to an accumulation of pollutants in the area. This accumulation pollutes the air and poses a risk to the local population. The presence of carbon monoxide in the southern region of Nigeria has been highlighted by the work of some authors.

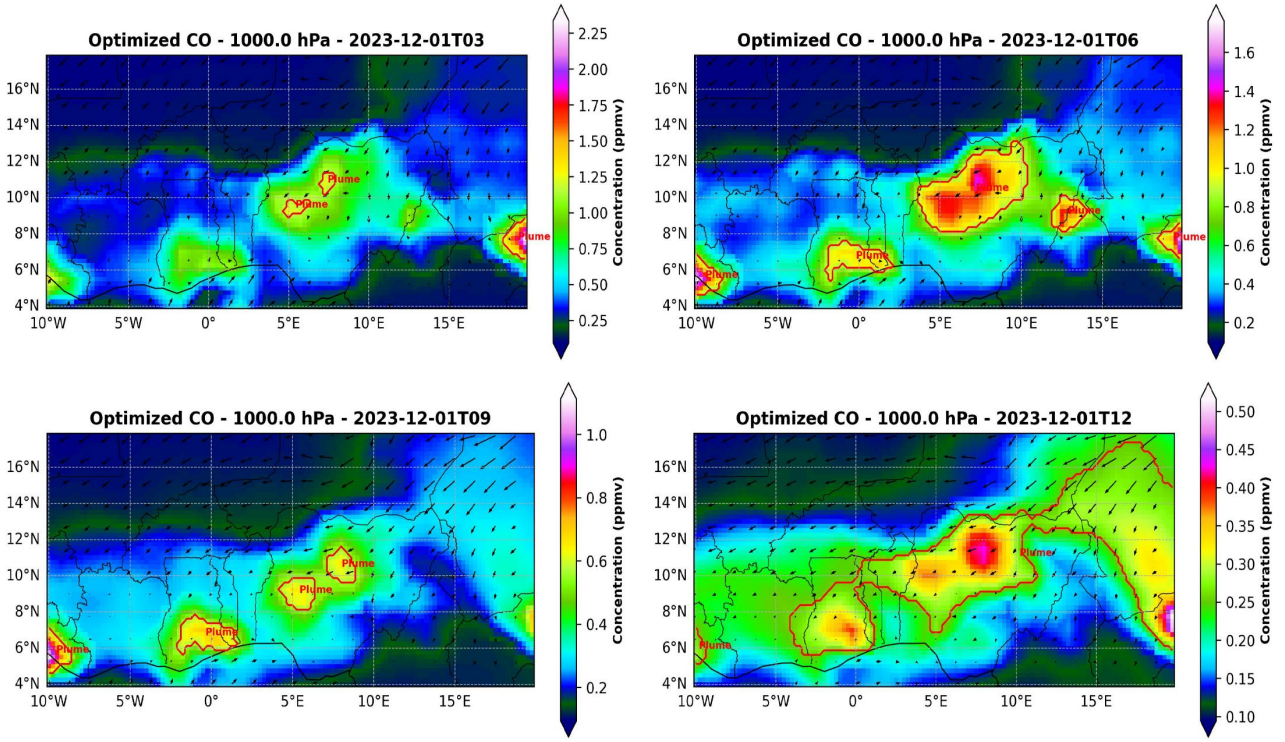

Figure 5. Temporal evolution of CO dispersion with interpolation of wind at 1000 hPa (Images generated by the Model-4D-Var).

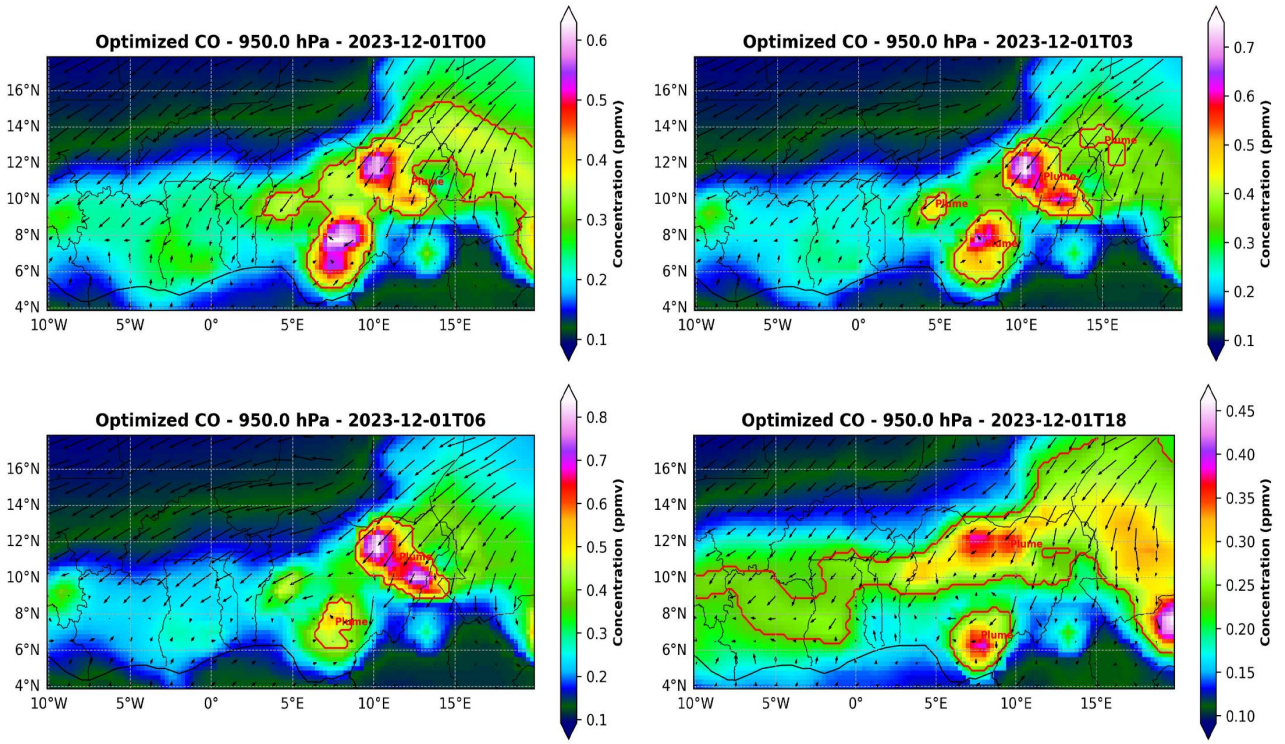

Figure 6. Temporal evolution of carbon monoxide dispersion with interpolation of wind at 950 hPa (Images generated by the Model-4D-Var).

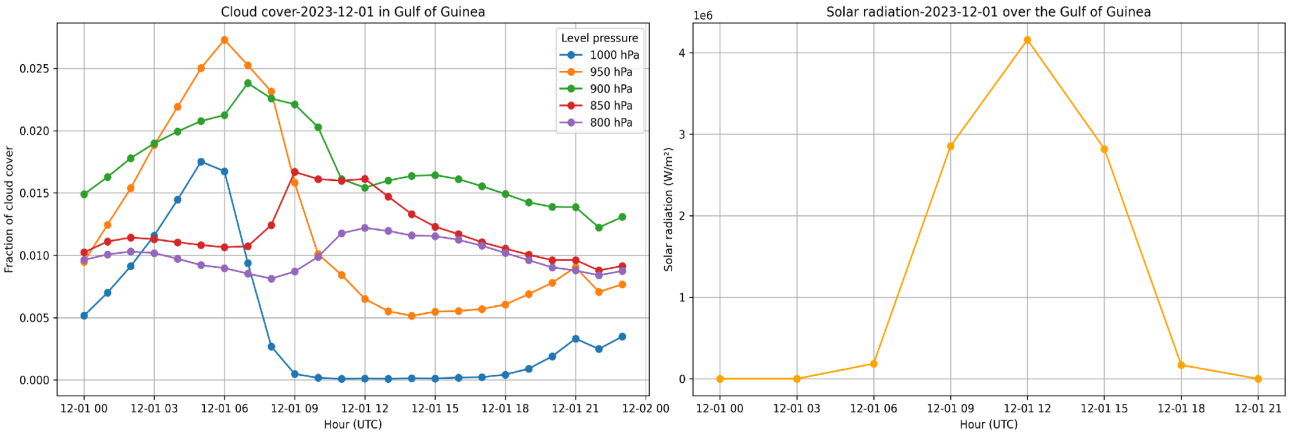

Figure 7. Illustration of cloud cover fraction and solar radiation.

Gijs et al. (2023) [2]; *Mayowa et al.* (2024) [3]; *Ajoke et al.* (2025) [4] highlighted the presence of carbon monoxide in southern and western Nigeria, caused by biomass burning and gas flaring, as well as by forest fires, incomplete combustion in road transport, residential heating and industry, and by transport and urbanization. An emission source located at *Warri* (5.33˚N, 5.36˚E) is specified by *Ajoke et al.* (2025) [4] in their work. This source detected at an altitude of 100 m near the ground helps to explain the origin of the plume identified by our model at an altitude of approximately 500m in this area.

3.2.2. Quantification of Continuous Vertical Plumes

Three plumes persisted at all altitudes considered in our study. They exhibited a spatio-temporal distribution with variability in concentration at each altitude.

- A plume identified north of *Nigeria*, near the city of *Kano*, whose origin is located near 9.30˚E and 12.30˚N. At 1000 hPa (**Figure 8**), it is less persistent between 00 h and 03 h but more persistent from 06 h onwards. We note a significant spatial occupation of the plume with a considerable concentration. The plume's distribution starts in northern Nigeria, crosses northern Benin from 12 h and extends to northern Togo. Starting at 950 hPa, the plume concentrates at its origin at 00 h with a molarity close to 0.6 ppmv. After 00 h, under the effect of a high-intensity dry wind, it disperses rapidly with a decrease in concentration. This means that a significant concentration of carbon monoxide is being emitted at a low altitude in northern Nigeria, and is visible from space. The results of the work carried out on the quantification of carbon monoxide from satellite images of *TROPOMI* (*Sentinel*-5 *Precusor*) by *Gijs et al.* (2023) [2], illustrate the presence of CO emission sources in the city of *Kano* (*Nigeria*) with an emission rate of 0.53 (0.41 - 0.62) Tg.yr^{-1}. The dispersion of the pollutant from these sources confirms the plumes represented by our model.
- A second plume has been detected in Ghana. Analysis of the wind circulation direction made it possible to locate an emission source which is located in the city of Kumasi (6.36˚N; 1.37˚W). This emission is due to transport, industrial

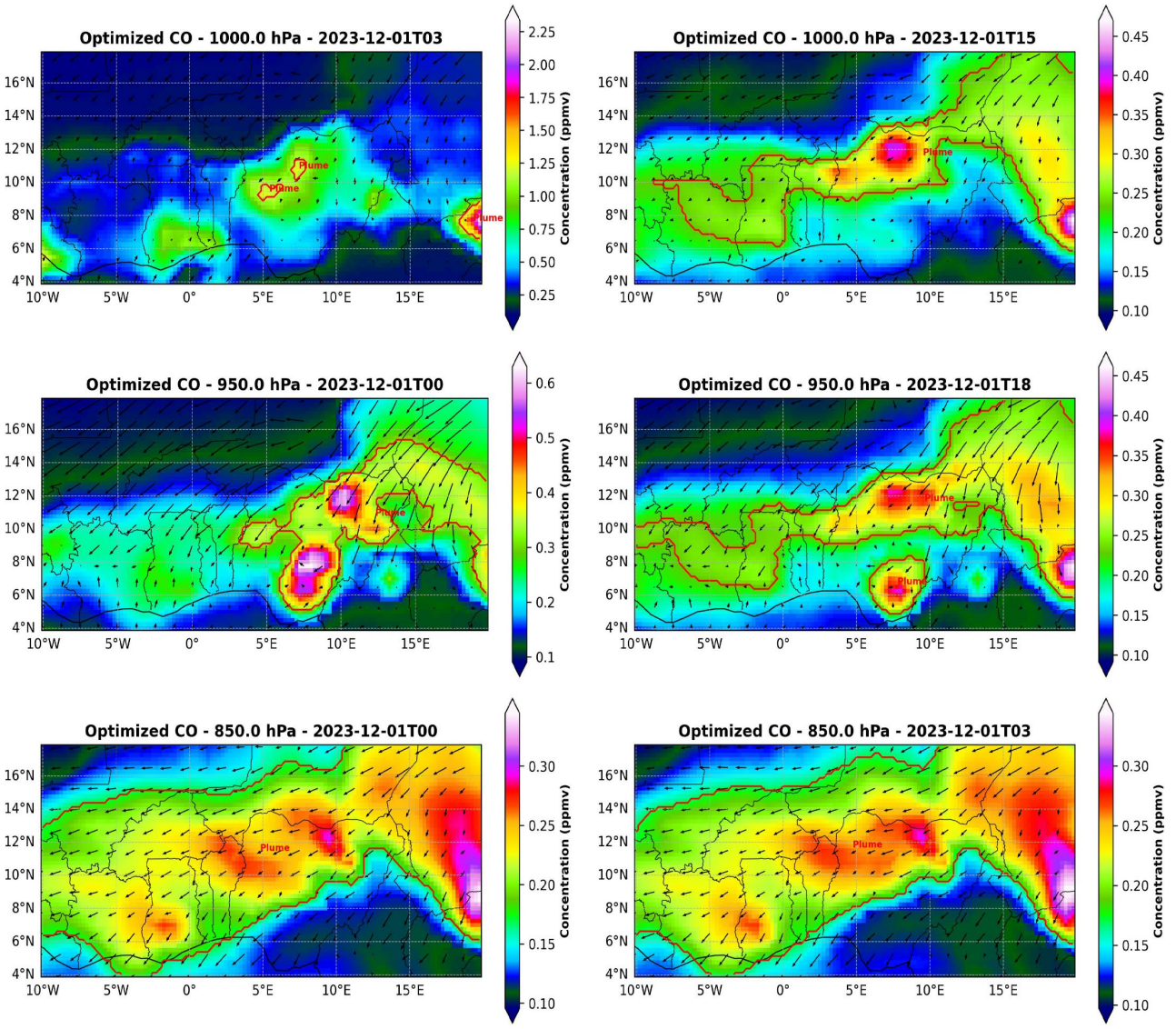

Figure 8. Temporal evolution of carbon monoxide dispersion with interpolation of wind at 1000 hPa and 950 hPa (Images generated by the Model-4D-Var).

- Activities and combustion. *Ajoke et al.* (2025) [4] indicated in their work, by approximation, the existence of a carbon monoxide emission source close to this city. The results of *Gijs et al.* (2023) [2] confirm the existence of a carbon monoxide emission source in the city of Kumasi. This result provides further details and confirms the presence of our plumes in this area. The dispersion of the pollutant emitted in this area is influenced by the wind from the Southwest at 1000 hPa. At low altitude (1000 hPa, **Figure 5**) between 03 h - 09 h, the pollutant disperses from the source, under the effect of the land breeze (south-west wind). It spreads south and extends south into Togo and Benin with a low concentration that varies between 1 ppmv - 1.5 ppmv.
- A third plume which is located in the Central African Republic, at 7.55˚N and 20˚E (**Figure 8**). It is located in an area characterized by the Sudanese savanna

and persists at all altitudes considered in this study. The dispersion of this plume influences the entire Gulf of Guinea area. It comes mainly from forest and agricultural fires [13]. At low altitudes, it is less present at night with a low concentration. However, during the day, a significant concentration of carbon monoxide is observed, which disperses into other countries and contributes to increasing the concentration of other plumes originating from other sources located in its direction. The distribution of this plume is strongly favored by the northeast wind. Onojeghuo *et al.* (2025) [4] indicated the presence of a source emitting this pollutant in this area.

4. Conclusions and Suggestions

This article involves the development of a theoretical and numerical model to explain the atmospheric dispersion of carbon monoxide in the Gulf of Guinea. Theoretically, the model is based on the scalar flux transport equation. The existence, uniqueness, and optimality conditions of this model are studied using the tools of control theory.

In practice, an analytical expression is derived from this theoretical model. This expression combines several parameters likely to influence the phenomenon of pollutant dispersion in the Gulf of Guinea. This analytical approach is coupled with a 4D-Var filter. The assimilation of ERA5 reanalysis data (horizontal and vertical wind, temperature, cloud cover, convection velocity, solar radiation, friction velocity) and carbon monoxide data from a coarse grid allowed the model to reproduce dispersion maps consistent with satellite images. The output maps have a higher resolution than satellite images. The consideration of atmospheric stratification and the variability of wind types in the Gulf of Guinea demonstrates the model's ability to adapt to the study area. The results obtained represent a significant contribution to the understanding of carbon monoxide transport in the Gulf of Guinea. Looking ahead, integrating the Kalman filter into the model will improve its future predictions.

Acknowledgements

The authors express their gratitude to the IMSP (Institut de Mathématiques et de Sciences Physiques) for providing its high-performance computing resources, which enabled the numerical simulations to be performed.

This research did not receive any specific funding from public, commercial, or non-profit funding organizations.

Conflicts of Interest

The authors declare no conflicts of interest regarding the publication of this paper.

References

[1] Philip, J.L., Richard, F. and Nereus, J.R. (2007) The Lancet Commission on Pollution and Health. *The Lancet*, **391**, 462-512.

[2] Leguijt, G., Maasakkers, J.D., Denier van der Gon, H.A.C., Segers, A.J., Borsdorff, T. and Aben, I. (2023) Quantification of Carbon Monoxide Emissions from African Cities Using Tropomi. *Atmospheric Chemistry and Physics*, **23**, 8899-8919. https://doi.org/10.5194/acp-23-8899-2023

[3] Mayowa, B.L. and Moboladji S.S. (2024) An Assessment of Carbon Monoxide Emission in Nigeria and Recommendations for Suustainable Mitigation Strategies on Climate impact. *FUTA Journal of Logistics and Innovation Technology*, **3**, Article 16.

[4] Onojeghuo, A., Fleming, Z.L., Panagi, M., Balzter, H. and Monks, P.S. (2025) Investigating the Dispersion and Transport of Carbon Monoxide in West Africa with a Focus on Biomass Burning and Gas Flaring Sources. *Discover Atmosphere*, **3**, Article No. 14. https://doi.org/10.1007/s44292-025-00038-6

[5] Koppmann, R.K., Czaplewski, V. and Reld, J.S. (2005) A Review of Biomass Burning Emissions, Part I: Gaseous Emissions of Carbon Monoxide, Methane, Volatile Organic Compounds, and Nitrogen Containing Compounds. *Atmospheric Chemistry and Physics Discussion*, **5**, 10455-10516.

[6] Logan, J.A., Jones, D.B.A., Livesey, N.J., Megretskaia, I., Carouge, C. and Nedelec, P. (2010) Analysis of CO in the Tropical Troposphere Using Aura Satellite Data and the GEOS-Chem Model: Insights into Transport Characteristics of the GEOS Meteorological Products. *Atmospheric Chemistry and Physics*, **10**, 12207-12232. https://doi.org/10.5194/acp-10-12207-2010

[7] Orina, F., Amukoye, E., Bowyer, C., Chakaya, J., Das, D., Devereux, G., *et al.* (2024) Household Carbon Monoxide (CO) Concentrations in a Large African City: An Unquantified Public Health Burden? *Environmental Pollution*, **351**, Article 124054. https://doi.org/10.1016/j.envpol.2024.124054

[8] Menut, L., Flamant, C., Turquety, S., Deroubaix, A., Chazette, P. and Meynadier, R. (2018) Impact of Biomass Burning on Pollutant Surface Concentrations in Megacities of the Gulf of Guinea. *Atmospheric Chemistry and Physics*, **18**, 2687-2707. https://doi.org/10.5194/acp-18-2687-2018

[9] Isichei, A.O., Muoghalu, J.I., Akeredolu, F.A. and Afolabi, O.A. (1995) Fuel Characteristics and Emissions from Biomass Burning and Land-Use Change in Nigeria. *Environmental Monitoring and Assessment*, **38**, 279-289. https://doi.org/10.1007/bf00546769

[10] Ichoku, C., Ellison, L.T., Willmot, K.E., Matsui, T., Dezfuli, A.K., Gatebe, C.K., *et al.* (2016) Biomass Burning, Land-Cover Change, and the Hydrological Cycle in Northern Sub-Saharan Africa. *Environmental Research Letters*, **11**, Article 095005. https://doi.org/10.1088/1748-9326/11/9/095005

[11] Abdelhak, B. (2016) Le Golfe de Guinée, zone de contrastes: Richesses et vulnérabilités. OCP Policy Center.

[12] Mir Alvarez, C., Hourcade, R., Lefebvre, B. and Pilot, E. (2020) A Scoping Review on Air Quality Monitoring, Policy and Health in West African Cities. *International Journal of Environmental Research and Public Health*, **17**, Article 9151. https://doi.org/10.3390/ijerph17239151

[13] Haslett, S.L., Taylor, J.W., Evans, M., Morris, E., Vogel, B., Dajuma, A., *et al.* (2019) Remote Biomass Burning Dominates Southern West African Air Pollution during the Monsoon. *Atmospheric Chemistry and Physics*, **19**, 15217-15234. https://doi.org/10.5194/acp-19-15217-2019

[14] Real, E., Orlandi, E., Law, K.S., Fierli, F., Josset, D., Cairo, F., *et al.* (2010) Cross-hemispheric Transport of Central African Biomass Burning Pollutants: Implications for Downwind Ozone Production. *Atmospheric Chemistry and Physics*, **10**, 3027-3046. https://doi.org/10.5194/acp-10-3027-2010

[15] Nicolas, M., Pierre, C. And Laurence, R. (2015) Paronama de la modélisation de la dispersion atmosphérique Atmospheric dispersion Models: An Overview. Pollution Atmosphérique.

[16] DeWitt, H.L., Gasore, J., Rupakheti, M., Potter, K.E., Prinn, R.G., Ndikubwimana, J.D.D., *et al.* (2019) Seasonal and Diurnal Variability in O_3, Black Carbon, and CO Measured at the Rwanda Climate Observatory. *Atmospheric Chemistry and Physics*, **19**, 2063-2078. https://doi.org/10.5194/acp-19-2063-2019

[17] Frédéric, D. (2012) Modélisation statistique des écoulements turbulents en convection forcée, mixte et naturelle. Thèse Mécanique des fluides. Université de Poitiers.

[18] Hersbach, H., Comyn-Platt, E., Bell, B., Berrisford, P., *et al.* (2023) ERA5 Post-Processed Daily-Statistics on Pressure Levels from 1940 to Present. Copernicus Climate Change Service (C3S) Climate Data Store (CDS).

[19] Inness, A., Ades, M., Agustí-Panareda, A., Barré, J., Benedictow, A., Blechschmidt, A., *et al.* (2019) The CAMS Reanalysis of Atmospheric Composition. *Atmospheric Chemistry and Physics*, **19**, 3515-3556. https://doi.org/10.5194/acp-19-3515-2019

[20] Brezis, H. (2011) Functional Analysis, Sobolev Spaces and Partial Differential Equations. Springer.

[21] Troltzsch, F. (2010) Optimal Control of Partial Differential Equations Theory, Methods and Application. American Mathematical society Providence.

[22] Schulze, B.W. and Wong, M.W. (2008) Pseudo-Differential Operators: Complex Analysis and Partial Differential Equations. Birkäuser Verlag.

[23] Chang, J.C. and Hanna, S.R. (2004) Air Quality Model Performance Evaluation. *Meteorology and Atmospheric Physics*, **87**, 167-196. https://doi.org/10.1007/s00703-003-0070-7

[24] Nino Ruiz, E.D. and Sandu, A. (2016) A Derivative-Free Trust Region Framework for Variational Data Assimilation. *Journal of Computational and Applied Mathematics*, **293**, 164-179. https://doi.org/10.1016/j.cam.2015.02.033

[25] Guedje, F.K., Houeto, A.V.V., Houngninou, E.B., Fink, A.H. and Knippertz, P. (2019) Climatology of Coastal Wind Regimes in Benin. *Meteorologische Zeitschrift*, **28**, 23-39. https://doi.org/10.1127/metz/2019/0930

[26] Lewellen, W.S., Teske, M. and Donaldson, C.D. (1973) Application of Turbulence Model Equations to Axisymmetric Wakes. *AIAA Journal*, **12**, 620-625. https://doi.org/10.2514/3.49308

[27] Hanna, T.R., Gary, A.B. and Rayford, P.H. (1981) Handbook on Atmospheric Diffusion, Atmospheric Turbulence and Diffusion Laboratory, National Oceanic and Atmosphere Admnistration. Technical Information Center U.S. Departement of Energy.

[28] Foulet, A. and Aissani, L. (2020) Caractérisation et évaluation de l'impact des odeurs en gestion de déchets. Jalon 22-1-Choix du modèle de dispersion. Centre pour la Communication Scientifique Directe.

[29] Batchelor, G. (1949) Diffusion in a Field of Homogeneous Turbulence. I. Eulerian Analysis. *Australian Journal of Scientific Research Series A*: *Physical Sciences*, **2**, 437-450. https://doi.org/10.1071/ch9490437

[30] Cirillo, M.C. and Poli, A.A. (1992) An Intercomparison of Semiempirical Diffusion Models under Low Wind Speed, Stable Conditions. *Atmospheric Environment*, **26**, 765-774. https://doi.org/10.1016/0960-1686(92)90236-e

[31] Pasquill, F. (1974) Atmospheric Diffusion: The Dispersion of Windbome Material from Industrial and Other Sources. Van Nostrand.

[32] Sharan, M. and Yadav, A.k. (1998) Simulation of Diffusion Experiments under Light Wind, Stable Conditions by a Variable K-Theory Model. *Atmospheric Environment*, **32**, 3481-3492. https://doi.org/10.1016/s1352-2310(98)00048-x

[33] Yeh, G.T. and Huang, C.H. (1975) Three-Dimensional Air Pollutant Modeling in the Lower Atmosphere. *Boundary-Layer Meteorology*, **9**, 381-390. https://doi.org/10.1007/bf00223389

[34] Park, S.K. and Liang, X. (2013) Data Assimilation for Atmospheric, Oceanic and Hydrologic Applications. Springer.

[35] Lenfle, S. (2018) De l'interpolation optimale au 4D-Var: L'émergence d'un nouveau dominant design en assimilation de données météorologiques. *La Météorologie*, **100**, 37-46. https://doi.org/10.4267/2042/65141

[36] Evensen, G., Vossepoel, F.C. and Van Leeuwen, P.J (2022) Data Assimilation Fundamentals: A Unified Formulation of State and Parameter Estimation Problem. Springer.

[37] Philip, D., Vishwas, R. and Mihai, A. (2025) Weakly-Constrained 4D-Var for Downscalling with Uncertainty Using Data-Driven Surrogate Models. https://arxiv.org/abs/2503.02665

[38] Klinker, E., Mahfouf, J. and Rabier, F. (2000) Une nouvelle technique d'assimilation des données d'observation au CEPMMT: L'assimilation variationnelle quadridimensionnelle. *La Météorologie*, **8**, 87-101. https://doi.org/10.4267/2042/36125

[39] Lions, J.L. (1968) Contrôle optimal des systèmes gouvernés par des équations aux dérivés partielles. Dunod/Gauthier-Villars (Paris).

[40] Le Dimet, F.X. and Talagrand, O. (1986) Variational Algorithms for Analysis and Assimilation of Meteorological Observations. *Dynamic Meteorology and Oceanography*, **38**, 97-110. https://doi.org/10.3402/tellusa.v38i2.11706

[41] Lewis, J.M. and Derber, J.C. (1985) The Use of Adjoint Equations to Solve a Variational Adjustment Problem with Advective Constraints. *Tellus A*: *Dynamic Meteorology and Oceanography*, **37**, 309-322. https://doi.org/10.3402/tellusa.v37i4.11675

[42] Derber, J.C. (1987) Variational Four-Dimensional Analysis Using Quasi-Geostrophic Constraints. *Monthly Weather Review*, **115**, 998-1008. https://doi.org/10.1175/1520-0493(1987)115<0998:vfdauq>2.0.co;2

[43] Courtier, P. and Talagrand, O. (1990) Variational Assimilation of Meteorological Observations with the Direct and Adjoint Shallow-Water Equations. *Tellus A*: *Dynamic Meteorology and Oceanography*, **42**, 531-554. https://doi.org/10.3402/tellusa.v42i5.11896

[44] Tikhonov, A. and Arsenin, V. (1977) Solutions of III Posed Problems. Washington.

[45] Nocedal, J. (1980) Updating Quasi-Newton Matrices with Limited Storage. *Mathematics of Computation*, **35**, 773-782. https://doi.org/10.1090/s0025-5718-1980-0572855-7

[46] Liu, D.C. and Nocedal, J. (1989) On the Limited Memory BFGS Method for Large Scale Optimization. *Mathematical Programming*, **45**, 503-528. https://doi.org/10.1007/bf01589116

[47] Akinyemi, M. (2012) Diminishing Atmospheric Carbon Monoxide Fluxes as a Forecast of the New Planting Season in West Africa. *American Journal of Scientific and Industrial Research*, **3**, 198-202. https://doi.org/10.5251/ajsir.2012.3.4.198.202

[48] Si, G.X., Fu, S.L. and Yao, W. (2024) Unlocking the Potential: Multi-Task Deep Learning for Spaceborne Quantitative Monitoring of Fugitive Methane Plumes.

[49] Groshenry, A., Giron, C., Lauvaux, T., d'Aspremont, A. and Ehret, T. (2022) Detecting Methane Plumes using PRISMA: Deep Learning Model and Data Augmentation. https://arxiv.org/abs/2211.15429v1

[50] Bertrand, R.L., Kerdreux, T., Tuel, A. and Claudia H. (2023) Autonomous Detection of Methane Emissions in Multispectral Satellite Data Using Deep Learning. https://arxiv.org/abs/2308.11003v1

[51] Wang, H.Z., Fan, X.T., Jian, H.D. and Yan, F. (2024) Exploiting the Matched Filter to Improve the Detection of Methane Plumes with Sentinel-2 Data. *Remote Sensing*, **16**, Article 1023. https://doi.org/10.3390/rs16061023

[52] Bruno, J.H., Jervis, D., Varon, D.J. and Jacob, D.J. (2024) U-Plume: Automated Algorithm for Plume Detection and Source Quantification by Satellite Point-Source Imagers. *Atmospheric Measurement Techniques*, **17**, 2625-2636. https://doi.org/10.5194/amt-17-2625-2024

[53] Monin, A. and Obukhov, A. (1954) Basic Laws of Turbulent Mixing in the Surface Layer of the Atmosphere. Contributions of the Geophysical Institute. *Academy of Sciences of the USSR*, **151**, 163-187.

[54] World Health Organisation (2021) WHO Global Air Quality Guidelines. Particulate Matter ($PM_{2.5}$ and PM_{10}), Ozone, Nitrogen Dioxide, Sulfur Dioxide and Carbon Monoxide. World Health Organisation.

[55] Bell, M.L., Peng, R.D., Dominici, F. and Samet, J.M. (2009) Emergency Hospital Admissions for Cardiovascular Diseases and Ambient Levels of Carbon Monoxide. *Circulation*, **120**, 949-955. https://doi.org/10.1161/circulationaha.109.851113

[56] Chen, R., Pan, G., Zhang, Y., Xu, Q., Zeng, G., Xu, X., *et al.* (2011) Ambient Carbon Monoxide and Daily Mortality in Three Chinese Cities: The China Air Pollution and Health Effects Study (CAPES). *Science of the Total Environment*, **409**, 4923-4928. https://doi.org/10.1016/j.scitotenv.2011.08.029

[57] Chen, K., Breitner, S., Wolf, K., Stafoggia, M., Sera, F., Vicedo-Cabrera, A.M., *et al.* (2021) Ambient Carbon Monoxide and Daily Mortality: A Global Time-Series Study in 337 Cities. *The Lancet Planetary Health*, **5**, e191-e199. https://doi.org/10.1016/s2542-5196(21)00026-7

[58] Samoli, E., Touloumi, G., Schwartz, J., Anderson, H.R., Schindler, C., Forsberg, B., *et al.* (2007) Short-term Effects of Carbon Monoxide on Mortality: An Analysis within the APHEA Project. *Environmental Health Perspectives*, **115**, 1578-1583. https://doi.org/10.1289/ehp.10375

Appendix A: Calculation and Minimization of Quantity: $\mathcal{L}(c_1)-\mathcal{L}(c_2)$

Let's calculate $\mathcal{L}(c_1)-\mathcal{L}(c_2)$:

$$\mathcal{L}(c_1)-\mathcal{L}(c_2)=K\frac{\mathrm{d}}{\mathrm{d}t}\left[\nabla(c_1-c_2)\right]+A\Delta(c_1-c_2)-\sigma^2\nabla(c_1-c_2)+B\nabla\Delta(c_1-c_2). \tag{40}$$

Let's calculate the *dot product* of this difference (40) in *Sobolev space*:

$$\begin{aligned}&\left\langle\mathcal{L}(c_1)-\mathcal{L}(c_2),(c_1-c_2)\right\rangle\\&=K\int_{\mathbb{Q}}\frac{\mathrm{d}}{\mathrm{d}t}\left[\nabla(c_1-c_2)\right](c_1-c_2)\mathrm{d}w+A\int_{\mathbb{Q}}\left[\Delta(c_1-c_2)\right](c_1-c_2)\mathrm{d}w\\&-\sigma^2\int_{\mathbb{Q}}\left[\nabla(c_1-c_2)\right](c_1-c_2)\mathrm{d}w+B\int_{\mathbb{Q}}\left[\nabla\Delta(c_1-c_2)\right](c_1-c_2)\mathrm{d}w.\end{aligned} \tag{41}$$

Let $(c_1-c_2)=h(t)g(x,y,z)$, with $h(t)\in[0,T]$ and $g(x,y,z)\in\Omega$, hence we obtain:

$$\begin{aligned}&\left\langle\mathcal{L}(c_1)-\mathcal{L}(c_2),(c_1-c_2)\right\rangle\\&=K\int_{\mathbb{Q}}\frac{\mathrm{d}h^2}{\mathrm{d}t}[\nabla g]g\mathrm{d}w+A\int_{\mathbb{Q}}\left[\Delta(hg)\right](hg)\mathrm{d}w\\&-\sigma^2\int_{\mathbb{Q}}\left[\nabla(hg)\right](hg)\mathrm{d}w+B\int_{\mathbb{Q}}\left[\nabla\Delta(hg)\right](hg)\mathrm{d}w\\&=K\int_{\Omega}[\nabla g]g\mathrm{d}\Omega\int_0^T\frac{\mathrm{d}h^2}{\mathrm{d}t}\mathrm{d}t+A\int_{\mathbb{Q}}\left[\Delta(hg)\right](hg)\mathrm{d}w\\&-\sigma^2\int_{\mathbb{Q}}\left[\nabla(hg)\right](hg)\mathrm{d}w+B\int_{\mathbb{Q}}\left[\nabla\Delta(hg)\right](hg)\mathrm{d}w\\&=\frac{K}{2}\int_{\Omega}[\nabla g]g\left[h^2\right]_0^T\mathrm{d}\Omega+A\int_{\mathbb{Q}}\left[\Delta(hg)\right](hg)\mathrm{d}w\\&-\sigma^2\int_{\mathbb{Q}}\left[\nabla(hg)\right](hg)\mathrm{d}w+B\int_{\mathbb{Q}}\left[\nabla\Delta(hg)\right](hg)\mathrm{d}w\end{aligned}$$

$$\begin{aligned}&\left\langle\mathcal{L}(c_1)-\mathcal{L}(c_2),(c_1-c_2)\right\rangle\\&=\frac{K}{2}\int_{\Omega}h^2T[\nabla g]g\mathrm{d}\Omega+A\int_{\mathbb{Q}}\left[\Delta(hg)\right](hg)\mathrm{d}w\\&-\sigma^2\int_{\mathbb{Q}}\left[\nabla(hg)\right](hg)\mathrm{d}w+B\int_{\mathbb{Q}}\left[\nabla\Delta(hg)\right](hg)\mathrm{d}w.\end{aligned} \tag{42}$$

We minimize each quantity of the scalar product (42). We suppose that $\lambda_i\in\mathbb{R}_+^*$, with $i=1,2,\cdots,n$:

$$\begin{aligned}&\lambda_1\le\Delta(hg)\le\lambda_2\\&\lambda_1(hg)\le\left[\Delta(hg)\right](hg)\le\lambda_2(hg)\\&A\int_{\mathbb{Q}}\lambda_1(hg)\mathrm{d}w\le A\int_{\mathbb{Q}}\left[\Delta(hg)\right](hg)\mathrm{d}w\le A\int_{\mathbb{Q}}\lambda_2(hg)\mathrm{d}w\\&\lambda_3\le\left[\nabla(hg)\right]\le\lambda_4\\&(hg)\lambda_3\le\left[\nabla(hg)\right](hg)\le\lambda_4(hg)\\&\int_{\mathbb{Q}}\lambda_3(hg)\mathrm{d}w\le\int_{\mathbb{Q}}\left[\nabla(hg)\right](hg)\mathrm{d}w\le\int_{\mathbb{Q}}\lambda_4(hg)\mathrm{d}w\end{aligned} \tag{43}$$

$$-\sigma^2\int_{\mathbb{Q}}\lambda_4(hg)\,\mathrm{d}w \le -\sigma^2\int_{\mathbb{Q}}\left[\nabla(hg)\right](hg)\,\mathrm{d}w \le -\sigma^2\int_{\mathbb{Q}}\lambda_3(hg)\,\mathrm{d}w \tag{44}$$

$$\lambda_5 \le \left[\nabla\Delta(hg)\right] \le \lambda_6$$

$$\int_{\mathbb{Q}}\lambda_5(hg)\,\mathrm{d}w \le \int_{\mathbb{Q}}\left[\nabla\Delta(hg)\right](hg)\,\mathrm{d}w \le \int_{\mathbb{Q}}\lambda_6(hg)\,\mathrm{d}w$$

$$B\int_{\mathbb{Q}}\lambda_5(hg)\,\mathrm{d}w \le B\int_{\mathbb{Q}}\left[\nabla\Delta(hg)\right](hg)\,\mathrm{d}w \le B\int_{\mathbb{Q}}\lambda_6(hg)\,\mathrm{d}w. \tag{45}$$

The combination of equations (43), (44) and (45) makes it possible to obtain a framework for the scalar product:

$$\begin{aligned}&\int_{\mathbb{Q}}\left\{A\lambda_1(hg)-\sigma^2\lambda_4(hg)+B\lambda_5(hg)\right\}\mathrm{d}w+\frac{K}{2}\int_{\Omega}h^2(T)[\nabla g]g\mathrm{d}\Omega\\ &\le\left\langle\mathcal{L}(c_1)-\mathcal{L}(c_2),(c_1-c_2)\right\rangle\\ &\le\int_{\mathbb{Q}}\left\{A\lambda_2(hg)-\sigma^2\lambda_3(hg)+B\lambda_6(hg)\right\}\mathrm{d}w+\frac{K}{2}\int_{\Omega}h^2(T)[\nabla g]g\mathrm{d}\Omega,\end{aligned} \tag{46}$$

hence

$$\begin{aligned}&\left\langle\mathcal{L}(c_1)-\mathcal{L}(c_2),(c_1-c_2)\right\rangle\\ &\ge\int_{\mathbb{Q}}\left\{A\lambda_1(hg)-\sigma^2\lambda_4(hg)+B\lambda_5(hg)\right\}\mathrm{d}w+\frac{K}{2}\int_{\Omega}h^2(T)[\nabla g]g\mathrm{d}\Omega\end{aligned} \tag{47}$$

$$\begin{aligned}&\left\langle\mathcal{L}(c_1)-\mathcal{L}(c_2),(c_1-c_2)\right\rangle\\ &\ge\int_{\mathbb{Q}}\left\{A\lambda_1-\sigma^2\lambda_4+B\lambda_5\right\}(hg)\,\mathrm{d}w+\frac{K}{2}\int_{\Omega}h^2(T)[\nabla g]g\mathrm{d}\Omega\end{aligned} \tag{48}$$

$$\left\langle\mathcal{L}(c_1)-\mathcal{L}(c_2),(c_1-c_2)\right\rangle \ge D\int_{\mathbb{Q}}(hg)\,\mathrm{d}w+K\int_{\mathbb{Q}}\frac{\mathrm{d}}{\mathrm{d}t}\left[\nabla(hg)\right](hg)\,\mathrm{d}w \tag{49}$$

$$\begin{aligned}&\left\langle\mathcal{L}(c_1)-\mathcal{L}(c_2),(c_1-c_2)\right\rangle\\ &\ge D\int_{\mathbb{Q}}(c_1-c_2)\,\mathrm{d}w+K\int_{\mathbb{Q}}\frac{\mathrm{d}}{\mathrm{d}t}\left[\nabla(c_1-c_2)\right](c_1-c_2)\,\mathrm{d}w\end{aligned} \tag{50}$$

$$\begin{aligned}&\left\langle\mathcal{L}(c_1)-\mathcal{L}(c_2),(c_1-c_2)\right\rangle\\ &\ge\min(D,K)\int_{\mathbb{Q}}\left\{\frac{\mathrm{d}}{\mathrm{d}t}\left[\nabla(c_1-c_2)\right](c_1-c_2)+(c_1-c_2)\right\}\mathrm{d}w\end{aligned} \tag{51}$$

$$\left\langle\mathcal{L}(c_1)-\mathcal{L}(c_2),(c_1-c_2)\right\rangle \ge \lambda_7\left\|c_1-c_2\right\|^2, \tag{52}$$

with $D=A\lambda_1-\sigma^2\lambda_4+B\lambda_5$ and $\lambda_7=\min(D,K)$.

Appendix B: Variation of Lagrange Functional

Let's $p\in\left[C_0^2(Q)\right]^3$ the adjoint variable and $c\in H(Q)$.

Remark: $\left[C_0^2(Q)\right]^3=C_0^2(Q)\times C_0^2(Q)\times C_0^2(Q)$. Let's δc and δc_0 be small variations of c and c_0.

$$\mathcal{A}(c,c_0;p)=\int_{\mathbb{Q}}L(c(t),c_0)\,\mathrm{d}w+\int_{\mathbb{Q}}\mathcal{M}(c,c_0)\cdot p\mathrm{d}w \tag{53}$$

$$\begin{aligned}&\mathcal{A}(c+\delta c,c_0+\delta c_0;p)\\ &=\int_{\mathbb{Q}}L(c+\delta c,c_0+\delta c_0)\,\mathrm{d}w+\int_{\mathbb{Q}}\mathcal{M}(c+\delta c,c_0+\delta c_0)\cdot p\mathrm{d}w\end{aligned} \tag{54}$$

The variation of Lagrange functional is:

$$\Delta\mathcal{A} = \mathcal{A}(c+\delta c, c_0+\delta c_0; p) - \mathcal{A}(c, c_0; p) \tag{55}$$

$$\begin{aligned} &= \int_{\mathbb{Q}} L(c+\delta c, c_0+\delta c_0)\,\mathrm{d}w + \int_{\mathbb{Q}} \mathcal{M}(c+\delta c, c_0+\delta c_0)\cdot p\,\mathrm{d}w \\ &- \int_{\mathbb{Q}} L(c, c_0)\,\mathrm{d}w - \int_{\mathbb{Q}} \mathcal{M}(c, c_0)\cdot p\,\mathrm{d}w \end{aligned} \tag{56}$$

$$\begin{aligned} &= \int_{\mathbb{Q}} \left\{ L(c+\delta c, c_0+\delta c_0) - L(c, c_0) \right\} \mathrm{d}w \\ &+ \int_{\mathbb{Q}} \left\{ \mathcal{M}(c+\delta c, c_0+\delta c_0) - \mathcal{M}(c, c_0) \right\} \cdot p\,\mathrm{d}w \end{aligned} \tag{57}$$

$$\Delta\mathcal{A} = \Delta\mathcal{A}_1 + \Delta\mathcal{A}_2, \tag{58}$$

with

$$\Delta\mathcal{A}_1 = \int_{\mathbb{Q}} \left\{ L(c+\delta c, c_0+\delta c_0) - L(c, c_0) \right\} \mathrm{d}w, \tag{59}$$

$$\Delta\mathcal{A}_2 = \int_{\mathbb{Q}} \left\{ \mathcal{M}(c+\delta c, c_0+\delta c_0) - \mathcal{M}(c, c_0) \right\} \cdot p\,\mathrm{d}w. \tag{60}$$

Lemma [20]: Let $c_0 \in L^{\infty}(\mathbb{Q})$ be the optimal control of the problem and c the corresponding state.

Then, the functional $\mathcal{A}_1$ is *Frechet differentiable* and the variation is expressed as:

$$\Delta\mathcal{A}_1 = \int_{\mathbb{Q}} \left[L_c(c, c_0)\delta c + L_{c_0}(c, c_0)\delta c_0 \right] \mathrm{d}w + o\left(\sqrt{\delta c^2 + \delta c_0^2} \right), \tag{61}$$

where L_c and L_{c_0} stand for the derivative with respect to c and c_0, respectively.

However, let us determine $\Delta\mathcal{A}_2$.

$$\mathcal{M}(c, c_0) = K\frac{\partial}{\partial t}(\nabla c) + A\Delta c - \sigma^2\nabla c + B\nabla\Delta c \tag{62}$$

$$\begin{aligned} &\mathcal{M}(c+\delta c, c_0+\delta c_0) \\ &= K\frac{\partial}{\partial t}\nabla(c+\delta c) + A\Delta(c+\delta c) - \sigma^2\nabla(c+\delta c) + B\nabla\Delta(c+\delta c) \end{aligned} \tag{63}$$

$$\begin{aligned} &\mathcal{M}(c+\delta c, c_0+\delta c_0) - \mathcal{M}(c, c_0) \\ &= K\frac{\partial}{\partial t}(\nabla\delta c) + A\Delta\delta c - \sigma^2\nabla\delta c + B\nabla\Delta\delta c. \end{aligned} \tag{64}$$

Then,

$$\begin{aligned} \Delta\mathcal{A}_2 &= \int_{\mathbb{Q}} K\frac{\partial}{\partial t}(\nabla\delta c)\cdot p\,\mathrm{d}w + \int_{\mathbb{Q}} A\Delta\delta c\cdot p\,\mathrm{d}w - \int_{\mathbb{Q}} \sigma^2\nabla\delta c\cdot p\,\mathrm{d}w \\ &+ \int_{\mathbb{Q}} B\nabla\Delta\delta c\cdot p\,\mathrm{d}w \end{aligned} \tag{65}$$

$$\begin{aligned} &= K\int_{\mathbb{Q}} \frac{\partial}{\partial t}(\nabla\delta c)\cdot p\,\mathrm{d}w + A\int_{\mathbb{Q}} \Delta\delta c\cdot p\,\mathrm{d}w - \sigma^2\int_{\mathbb{Q}} \nabla\delta c\cdot p\,\mathrm{d}w \\ &+ B\int_{\mathbb{Q}} \nabla\Delta\delta c\cdot p\,\mathrm{d}w \end{aligned} \tag{66}$$

$$= E_1 + E_2 - E_3 + E_4 \tag{67}$$

where:

$$E_1 = K\int_{\mathbb{Q}} \frac{\partial}{\partial t}(\nabla\delta c)\cdot p\,\mathrm{d}w \tag{68}$$

$$E_2 = A\int_{\mathbb{Q}} \Delta\delta c \cdot p \mathrm{d}w \tag{69}$$

$$E_3 = \sigma^2 \int_{\mathbb{Q}} \nabla\delta c \cdot p \mathrm{d}w \tag{70}$$

$$E_4 = B\int_{\mathbb{Q}} \nabla\Delta\delta c \cdot p \mathrm{d}w \tag{71}$$

We calculate expressions (68)-(71) by partial integration. The following assumption is satisfied: $p(T) = 0$

$$E_1 = K\int_{\Omega} \nabla \int_0^T \frac{\partial \delta c}{\partial t} \cdot p \mathrm{d}t \mathrm{d}\Omega \tag{72}$$

$$E_1 = K\int_{\Omega} \nabla \left[\left[(\delta c)\, p \right]_0^T - \int_0^T \frac{\partial p}{\partial t} \delta c \mathrm{d}t \right] \mathrm{d}\Omega \tag{73}$$

$$E_1 = -K\int_{\Omega} \nabla \delta c_0 \cdot p(0) \mathrm{d}\Omega - K\int_{\Omega} \nabla \int_0^T \frac{\partial p}{\partial t} \delta c \mathrm{d}t \mathrm{d}\Omega \tag{74}$$

$$E_1 = K\int_{\Omega} \nabla p(0) \delta c_0 \mathrm{d}\Omega - K\int_{\mathbb{Q}} \nabla \frac{\partial p}{\partial t} \delta c \mathrm{d}w. \tag{75}$$

Referring to Green's transformation, we obtain:

$$E_2 = A\int_{\mathbb{Q}} \Delta\delta c \cdot p \mathrm{d}w \tag{76}$$

$$= A\int_{\mathbb{Q}} \delta c \Delta p \mathrm{d}w + \int_{\partial\Omega} \left(p\partial_n \delta - \delta c \partial_n p \right) \mathrm{d}\Omega \tag{77}$$

$$E_2 = A\int_{\mathbb{Q}} \Delta p \delta c \mathrm{d}w. \tag{78}$$

By analogy

$$E_3 = -\sigma^2 \int_{\mathbb{Q}} \nabla p \cdot \delta c \mathrm{d}w \tag{79}$$

$$E_4 = B\int_{\mathbb{Q}} \Delta(\nabla p) \delta c \mathrm{d}w \tag{80}$$

Thus, from expressions (75)-(80), we obtain:

$$\begin{aligned} \Delta\mathcal{A}_2 = {} & K\int_{\Omega} \nabla p(0) \delta c_0 \mathrm{d}\Omega - K\int_{\mathbb{Q}} \nabla \frac{\partial p}{\partial t} \delta c \mathrm{d}w + A\int_{\mathbb{Q}} \Delta p \delta c \mathrm{d}w \\ & + \sigma^2 \int_{\mathbb{Q}} \nabla p \cdot \delta c \mathrm{d}w + B\int_{\mathbb{Q}} \Delta(\nabla p) \delta c \mathrm{d}w. \end{aligned} \tag{81}$$

The introduction of the terms (61) and (81) into (59) gives:

$$\begin{aligned} \Delta\mathcal{A} = {} & \int_{\mathbb{Q}} \left[L_c(c, c_0) \delta c + L_{c_0}(c, c_0) \delta c_0 \right] \mathrm{d}w - K\int_{\mathbb{Q}} \nabla \frac{\partial p}{\partial t} \delta c \mathrm{d}w \\ & + A\int_{\mathbb{Q}} \Delta p \delta c \mathrm{d}w + \sigma^2 \int_{\mathbb{Q}} \nabla p \cdot \delta c \mathrm{d}w + K\int_{\Omega} \nabla p(0) \delta c_0 \mathrm{d}\Omega \\ & + B\int_{\mathbb{Q}} \Delta(\nabla p) \delta c \mathrm{d}w + o\left(\sqrt{\delta c^2 + \delta c_0^2} \right) \end{aligned} \tag{82}$$

$$\begin{aligned} \Delta\mathcal{A} = {} & \int_{\mathbb{Q}} \left[L_c(c, c_0) - K\nabla \frac{\partial p}{\partial t} + A\Delta p + \sigma^2 \nabla p + B\Delta(\nabla p) \right] \delta c \mathrm{d}w \\ & + o\left(\sqrt{(\delta c)^2 + (\delta c_0)^2} \right) + \int_{\Omega} \left[\int_0^T L_{c_0}(c, c_0) \mathrm{d}t + K\nabla p(0) \right] \delta c_0 \mathrm{d}\Omega \end{aligned} \tag{83}$$

Appendix C: Analytical Solution

We consider the equation (2) with assumptions 1, 2, 3, 4 and 5. We choose the Fourier transforms method.

Let $c(x,y,z,t) = c_x(x,t)c_y(y,t)c_z(z,t)$

with $c_x(x,0) = S^{1/3}\delta(x)$, $c_y(y,0) = S^{1/3}\delta(y)$, $c_x(z,0) = S^{1/3}\delta(z-H)$.

This separation of variables makes it possible to obtain the following equations:

$$K_x \frac{\partial}{\partial t}\left(\frac{\partial c_x}{\partial x}\right) + A_x \frac{\partial^2 c_x}{\partial x^2} - \sigma_u^2 \frac{\partial c_x}{\partial x} + B_x \frac{\partial^3 c_x}{\partial x^3} = 0, \tag{84}$$

$$K_y \frac{\partial}{\partial t}\left(\frac{\partial c_y}{\partial y}\right) + A_y \frac{\partial^2 c_y}{\partial y^2} - \sigma_v^2 \frac{\partial c_y}{\partial y} + B_y \frac{\partial^3 c_y}{\partial y^3} = 0, \tag{85}$$

$$K_z \frac{\partial}{\partial t}\left(\frac{\partial c_z}{\partial z}\right) + A_z \frac{\partial^2 c_z}{\partial z^2} - \sigma_w^2 \frac{\partial c_z}{\partial z} + B_z \frac{\partial^3 c_z}{\partial z^3} = 0. \tag{86}$$

We consider the equation (84), and by *Fourier transform*, we suppose that:

$$c_x(x,t) = \mathcal{F}^{-1}\left\{\tilde{c}(\eta,t)\right\} = \frac{1}{\sqrt{2\pi}}\int_{-\infty}^{+\infty} \widetilde{c_x}(\eta,t)\exp(i\eta x)\,\mathrm{d}\eta, \tag{87}$$

$$\widetilde{c_x}(\eta,t) = \mathcal{F}\left\{c_x(x,t)\right\} = \frac{1}{\sqrt{2\pi}}\int_{+\infty}^{-\infty} c_x(x,t)\exp(-i\eta x)\,\mathrm{d}x. \tag{88}$$

The introduction of formulas (87) into the equation (84) gives:

$$K_x \frac{\partial\left(i\eta\widetilde{c_x}\right)}{\partial t} - \eta^2 A_x \widetilde{c_x} - \sigma_u^2\left(i\eta\widetilde{c_x}\right) + B_x\left(-i\eta^3\widetilde{c_x}\right) = 0, \tag{89}$$

$$\widetilde{c_x}(\eta,t) = \beta_1 \exp\left\{\left[\frac{A_x}{K_x}\eta + i\left(\frac{\sigma_u^2}{K_x}\eta + \frac{B_x}{K_x}\eta^2\right)\right]t\right\}. \tag{90}$$

For $t = 0$ we have:

$$\widetilde{c_x}(\eta,t) = \frac{S^{1/2}}{\sqrt{2\pi}}\exp\left\{\left[\frac{A_x}{K_x}\eta + i\left(\frac{\sigma_u^2}{K_x}\eta + \frac{B_x}{K_x}\eta^2\right)\right]t\right\}. \tag{91}$$

The inverse of this transform (91) is:

$$c_x(x,t) = \frac{S^{1/2}}{2\sqrt{\pi}} \times \sqrt{\frac{K_x}{B_x t}} \times \exp\left\{-\left[\frac{\left(x + \frac{A_x t}{K_x} + \frac{\sigma_u^2 t}{K_x}\right)^2}{-\frac{4B_x t}{K_x}}\right]\right\}. \tag{92}$$

By analogy, we obtain:

$$c_x(x,t) = \frac{S^{1/2}}{2\sqrt{\pi}} \times \sqrt{\frac{K_x}{B_x t}} \times \exp\left[\frac{\left(x + \frac{A_x t}{K_x} + \frac{\sigma_u^2 t}{K_x}\right)^2}{\frac{4B_x t}{K_x}}\right], \tag{93}$$

$$c_y(y,t) = \frac{S^{1/2}}{2\sqrt{\pi}} \times \sqrt{\frac{K_y}{B_y t}} \times \exp\left[\frac{\left(y + \frac{A_y t}{K_y} + \frac{\sigma_v^2 t}{K_y}\right)^2}{\frac{4B_y t}{K_y}}\right], \tag{94}$$

$$c_z(z,t) = \frac{S^{1/2}}{2\sqrt{\pi}} \times \sqrt{\frac{K_z}{B_z t}} \times \exp\left[\frac{\left((z-H) + \frac{A_z t}{K_z} + \frac{\sigma_w^2 t}{K_z}\right)^2}{\frac{4B_z t}{K_z}}\right]. \tag{95}$$

Thus, with the initial conditions, we obtain the following analytical solution:

$$c(x,y,z,t) = \frac{q}{8\bar{u}(\pi t)^{3/2}} \times \sqrt{\frac{K_x K_y K_z}{B_x B_y B_z}} \times \exp\left[\frac{\left(xK_x + A_x t + \sigma_u^2 t\right)^2}{\left(4B_x t\right)} + \frac{\left(yK_y + A_y t + \sigma_v^2 t\right)^2}{\left(4B_y t\right)} + \frac{\left(K_z(z) + A_z t + \sigma_w^2 t\right)^2}{4B_z t}\right]. \tag{96}$$

Appendix D: FAC2 Values for Each Pressure Level as a Function of Time

Table A1. FAC2 for each pressure level as a function of time.

Pressure (hPa)	00 h	03 h	06 h	09 h	12 h	15 h	18 h	21 h
1000	0.498	0.486	0.489	0.633	0.736	0.778	0.648	0.551
950	0.691	0.686	0.691	0.699	0.738	0.782	0.756	0.731
900	0.761	0.758	0.767	0.782	0.768	0.801	0.803	0.799
850	0.840	0.832	0.830	0.828	0.835	0.848	0.856	0.858
800	0.925	0.923	0.923	0.911	0.906	0.909	0.910	0.910